HYBRID LASER INTEGRATION FOR SILICON PHOTONICS PLATFORM

by

Shuyu Yang

A dissertation submitted to the Faculty of the University of Delaware in partial fulfillment of the requirements for the degree of Doctor of Philosophy in Electrical and Computer Engineering

Spring 2015

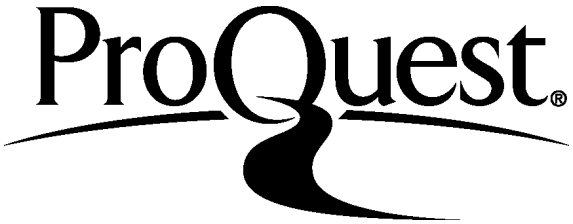

HYBRID LASER INTEGRATION FOR SILICON PHOTONICS PLATFORM

by

Shuyu Yang

Approved: _____
Kenneth E. Barner, Ph.D.
Chair of the Department of Electrical and Computer Engineering

Approved: _____
Babatunde A. Ogunnaike, Ph.D.
Dean of the College of Engineering

Approved: _____
James G. Richards, Ph.D.
Vice Provost for Graduate and Professional Education

I certify that I have read this dissertation and that in my opinion it meets the academic and professional standard required by the University as a dissertation for the degree of Doctor of Philosophy.

Signed: _____

Mark Mirotznik, Ph.D.
Professor in charge of dissertation

I certify that I have read this dissertation and that in my opinion it meets the academic and professional standard required by the University as a dissertation for the degree of Doctor of Philosophy.

Signed: _____

Keith Goossen, Ph.D.
Member of dissertation committee

I certify that I have read this dissertation and that in my opinion it meets the academic and professional standard required by the University as a dissertation for the degree of Doctor of Philosophy.

Signed: _____

Garrett Schneider, Ph.D.
Member of dissertation committee

I certify that I have read this dissertation and that in my opinion it meets the academic and professional standard required by the University as a dissertation for the degree of Doctor of Philosophy.

Signed: _____

Michael Hochberg, Ph.D.
Member of dissertation committee

ACKNOWLEDGMENTS

I would like to gratefully and sincerely thank Professor Mark Mirotznik and Michael Hochberg for their support and guidance during my graduate study.

Besides my advisors, I would like to thank the rest of my thesis committee: Dr. Keith Goossen and Dr. Garrett Schneider for their insightful comments. I must acknowledge Dr. Keith Goossen, who offered the course "Optical Properties of Solids", which was one of the most interesting classes I had a chance to take at University of Delaware and it really helped me gain a solid understanding of the fundamentals in this field.

A very special thanks goes out to Dr. Yi Zhang for his patience, motivation and continuous encouragement as well as the collaboration on the projects. I appreciate Dr. Dave Grund and Garrett Ejzak's help in building my laser test setup. I would also like to thank Dr. Yang Liu, Dr. Tom Baehr-Jones, and other students in our lab group for their advices and useful discussions. I also acknowledge Xiaoliang Zhu, Qi Li in Professor Keren Bergman's group in Columbia University for their assistance in device testing.

Finally, and most importantly, I would like to thank my parents and sisters for their support, encouragement, unwavering love, and belief in me. Thanks to my niece, Sophia, for her sweet and angelic smile which always reminds me of love, kind, beauty of life. I would also like to thank my friends both in China and here in US for adding truckloads of joy and happiness through the years.

DEDICATION

To my family

TABLE OF CONTENTS

LIST OF TABLES

LIST OF FIGURES

ABSTRACT

Silicon photonics has attracted extensive attention in both academia and industry in recent years, as an enabling technology to address the exponentially increasing demands for communication bandwidth. It brings state-of-the-art complementary metal-oxide-semiconductor (CMOS) processing technology to the field of photonic integration. The high yield and uniformity of silicon devices make it possible to build complex photonic systems-on-chip in large production volumes. Cutting-edge device performance has been demonstrated on this platform, including high-speed modulators, photodetectors, and passive devices such as the Y-junction, waveguide crossing, and arrayed waveguide gratings. As the device library quickly matures, an integrated laser source for a transmitter remains missing from the design kit.

I demonstrated hybrid external cavity lasers by integrating reflective optical semiconductor amplifiers and silicon photonics chips. The gain chip and silicon chip can be designed and optimized independently, which is a significant advantage compared to bonding an III-V film on top of the silicon chip. Advanced optoelectronics packaging processes can be leveraged for chip alignment. Tunable C-Band (near 1550 nm) lasers with 10 mW on-chip power and less than 220 kHz bandwidth are demonstrated. O-Band lasers (operating near 1310 nm) as well as successful data transmission at 10 Gb/s and 40 Gb/s using the hybrid laser as the light source are also demonstrated. I designed a single cavity, multi wavelength laser by utilizing a quantum dot SOA, Sagnac loop and micro-ring based silicon photonics half

cavity. Four lasing peaks with less than 3 dB power non-uniformity were measured, as well as 4 × 10 Gb/s error free data transmission.

In addition to my main focus on RSOA/Silicon external cavity lasers, I propose and demonstrate a novel germanium-assisted grating coupler with low loss on-and-off chip fiber coupling. A coupling efficiency of 76% at 1.55 μm and 40 nm 1 dB optical bandwidth is achieved using FDTD simulation.

Chapter 1

INTRODUCTION

The last decade witnessed substantial progress in research and early commercialization in the area of silicon photonics [1-8]. It leverages silicon processing technology developed by the IC industry, which supports large wafer, high device yield and performance uniformity. The exponentially growing traffic on the Internet calls for innovative ways to deliver data in metro and long haul optical networks, as well as intra-and-inter warehouse scale data centers. The high speed, low energy consumption, and low cost silicon photonics transceivers meet this requirement. In Chapter 1, I will first review state-of-the-art status of silicon photonics technology, with a focus on approaches on laser integration. An outline of the thesis is given at the end of this chapter. This thesis is based largely on research work I took a lead on and published as first author. For collaborative research, the division between the work of others and my contribution is explained.

1.1 Silicon Waveguides

The band gap of silicon is 1.1 eV, corresponding to an absorption wavelength up to 1.11 μm, which means it is transparent in the telecom wavelength window, 1.3 μm to 1.6 μm, making it viable as a photonics integrated circuits (PIC) material in addition to being the dominant electronics chip substrate. Moreover, the high index contrast between silicon and silicon oxide, 3.4 to 1.4, enables submicron waveguide width with strong confinement and low bending loss, even for a bend radius of only a

few micrometers. Waveguide propagation loss, which is mainly due to light scattering at imperfectly smooth sidewalls created by dry etching, has been reduced from over 10 dB/cm [9] in the early days to 0.026 dB/cm [10] as a result of both waveguide design and process optimization. A number of compact and efficient passive devices have been developed, including Y-junctions, waveguide crossings, grating couplers, arrayed waveguide gratings etc.

1.2 Silicon Electro-optic Modulators

On the other hand, because the silicon lattice is centrally symmetric, it doesn't have direct electro-optic (EO) effect, making it hard to build a modulator. Fortunately the refractive index of silicon varies with its free carrier concentration, also known as free carrier plasma dispersion effect, can be utilized for modulation [3]. Typical implementation of EO modulators on silicon includes doping a rib waveguide to form a pn junction, which overlaps with the optical mode. The junction depletion region width, thus the waveguide effective index and phase of the guided optical signal, can then be modulated by an electric voltage signal. In addition to a pn junction, a MOS capacitor biased in accumulation region can also be used to modulate silicon waveguide effective index.

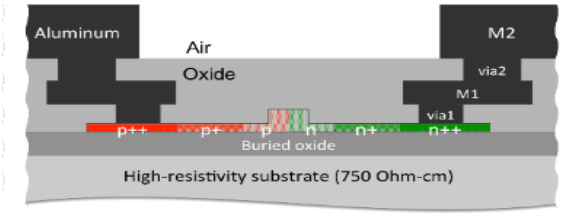

Figure 1.1 Cross section of a pn junction silicon modulator.

Phase change can be converted to intensity modulation by interference, either with a Mach Zehnder interferometer (MZI) or ring resonators. MZI modulators are broadband and robust against fabrication or temperature variations. However, because free carrier plasma dispersion is a weak effect, the MZI needs to be a few millimeters long for effective phase modulation, which leads to a large junction capacitance. To reduce the RC time limitation on device bandwidth, the modulator electrodes are usually designed as a travelling wave coplanar transmission line. On the other hand, ring modulators are extremely compact, with radius less than 10 μm, and as a result very energy efficient. However, due to the nature of ring resonance, ring modulators are optically narrow band and are sensitive to fabrication and temperature perturbations. Peripheral control circuits are necessary to maintain the resonant wavelength against ambient temperature change.

1.3 Ge-on-Si Photodetector

Apart from its lack of direct EO effect, silicon is an indirect band gap material, and transparent in the near infrared, thus it is intrinsically challenging to build lasers and photodetectors in silicon. We will discuss photodetectors first. It has been shown that silicon waveguides with defects introduced by ion implantation (without subsequent annealing) contain mid-gap energy states, which can serve as a stepping stone for photon absorption and can be used for detection [11]. Absorption by defect states extends beyond near infrared (IR) and is sometimes utilized for mid-IR applications. However the responsivity of photodetectors of this type is too low to be used in optical receivers. At the same time, implantation defects are sensitive to elevated temperatures greater than 300 °C, which requires the implantation step to be the very end of the fabrication process and imposes constrains on packaging solutions.

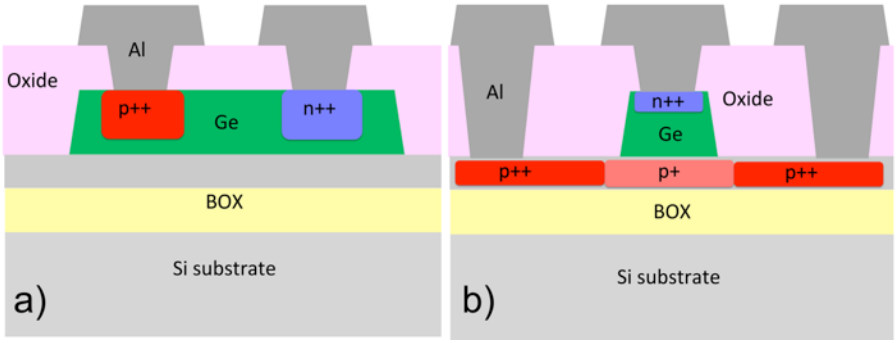

Figure 1.2 Lateral (a) and vertical (b) *p-i-n* Ge-on-Si photodetectors.

The mainstream approach is to use germanium that is epitaxially grown on silicon as the light absorbing material [4]. Germanium is CMOS compatible, with a direct band gap of 0.8 eV, corresponding to a photon wavelength of 1.54 µm. A two-step growth method mitigates the lattice mismatch between silicon and germanium and produces germanium crystals with low defect density. Ge-on-Si photodetectors with responsivities higher than 0.8 A/W, bandwidth greater than 30 GHz, and dark current less than a few µAs have been demonstrated [12-15]. The detector responsivity and bandwidth are comparable to their III-V counterparts. Although the dark current is higher than that in InGaAs detectors, they donot limit the sensitivity of a receiver since the electronic pre-amplifier (trans-impedance amplifier or TIA) noise dominates.

Recently we demonstrated a novel and high performance photodetector as shown in Fig. 1.3 [16]. Due to the difference in growth rate of different crystal orientations, a narrow strip of germanium, 1 µm in this case, forms a triangular cross section. A pn junction is formed in the silicon waveguide beneath the germanium, similar to the pn junction used for modulation in Fig. 1.1. Since the silicon is very thin and germanium has a higher permittivity, the fringe junction field is enough to sweep the carriers out at reasonable reverse bias voltages <4 V. Note that making good metal

contacts is a complicated process module in CMOS, typically requiring implantation, annealing, contact hole opening, silicide formation, diffusion barrier deposition, metal deposition, patterning, and planarization. Since the design has no metal in direct contact with the germanium, no additional metal-contact process is needed and the fabrication process is significantly simplified. And since there is no doping of the germanium, the fabrication process is again simpler than other detector designs. Actually only a germanium epitaxy step is needed in addition to a modulator-only flow.

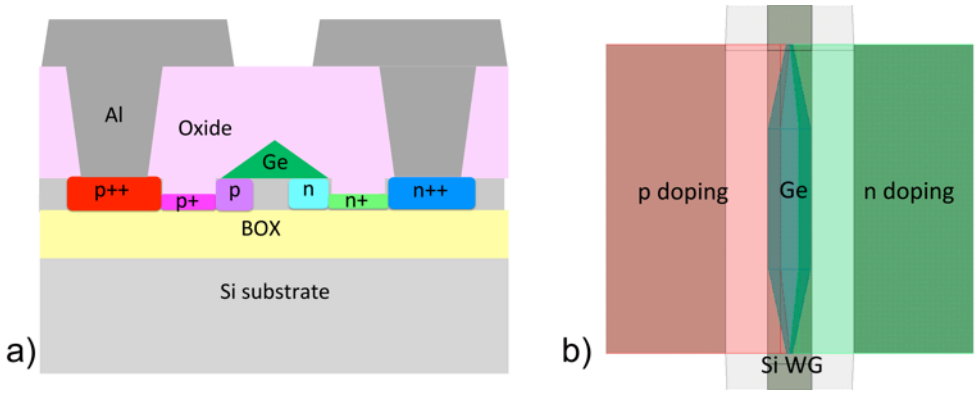

Figure 1.3 Germanium photodetector that doesn't require doping the germanium and avoids direct contact between the germanium and metals: a) cross section, and b) device layout (plan view).

Despite the simplified fabrication, this device demonstrates better performance than those in Fig. 1.2, or references 12-15. Because there are no defects introduced with ion implantation or metal deposition, the germanium crystal quality is preserved post epitaxy. When a taper is used, as shown in Fig. 1.3(b), the device maintains single mode operation. The optical mode is tightly confined in the germanium part, which

helps absorption. The device was measured to have 1.14 A/W responsivity at 1.55μm, 0.1 μA dark current and over 20 GHz bandwidth at -4 V. If a higher bias voltage of -12 V is available, the bandwidth would increases to over 40 GHz, and responsivity improves to 1.44 A/W due to the turn-on of avalanche multiplication, but dark current is still under 1 μA.

1.4 Laser Integration on Silicon

1.4.1 Optically pumped Raman and Erbium lasers

Laser integration is one of the most challenging tasks in silicon photonics. To the first order, a laser consists of a gain block in a resonant cavity. Since silicon is an indirect band gap material, a gain medium of another material has to be properly integrated into the CMOS material system. Early efforts utilized Raman nonlinearity or Erbium doping to achieve gain in silicon or silicon dioxide. Optically pumped monolithic Raman and Erbium lasers were successfully demonstrated [17-18]. However because of the large mode mismatch between submicron silicon waveguides and typical semiconductor laser or optical fiber modes, the on-chip coupling loss is usually greater than 1 dB. That loss together with the limited efficiency of an optically pumped laser, makes them less competitive compared to a directly coupled laser source at the desired wavelength. Hence an efficient electrically pumped laser is strongly preferred.

1.4.2 Germanium and quantum dot lasers

A number of approaches for integrating external gain media have been reported, including heterogeneous epitaxy, wafer bonding, and gain chip edge coupling [19-25]. Monolithic integration by epitaxy provides multiple advantages: 1)

epitaxy is a wafer-scale process, thus cost-effective; 2) high integration density; 3) gain section can be placed anywhere on the chip; 4) the connections between the gain section and other devices are lithographically defined so no extra alignment is needed.

In the previous section, we've mentioned that epitaxial germanium has been used for photodetectors, and is CMOS compatible. It is worthwhile to take a closer look at its band diagram. The difference between its direct band gap, Γ valley, and indirect band gap, L valley, is small, only 136 meV. The germanium is relaxed and in equilibrium at the elevated growth temperature. During cooling down to room temperature, tensile strain accumulates due to the different thermal expansion coefficients of silicon and germanium. This tensile strain further reduces the band gap difference. The rest of differences between direct and indirect band gap can be compensated by filling electrons into the L valley via n-type doping, thus turning germanium into a direct-band-gap like material. An electrically-pumped laser using heavily n-doped epitaxial Germanium was demonstrated by Camacho-Aguilera et al in 2012 [19]. Over 1 mW on chip output power and greater than 100 nm gain spectrum were reported. However, the threshold current of this device is extremely high (~280kA/cm^2). In addition to tensile strain and n-type doping, alloying with Tin has been demonstrated as another approach to convert germanium into a direct band gap material [26-27].

Besides germanium, efforts to grow conventional III-V quantum well materials on silicon have also been reported [20]. However, compared to Germanium, III-V on silicon heterogeneous epitaxy has much lower CMOS compatibility. But such lasers had poor performance due to a high density of dislocations due to the lattice mismatch. Recently, it was shown that this issue can be mitigated by replacing the quantum well

active region with quantum dots. The strong carrier confinement of and localization within a quantum dot can effectively shield carriers from dislocation. Although the research is encouraging, monolithic lasers are still in their infancy, and the efficiency and/or yield is still too low for practical applications.

1.4.3 Heterogeneous laser integration by III-V wafer bonding

Monolithic lasers are most desirable, but are also the most technically challenging. A second approach that mimics monolithic integration is wafer bonding. The silicon on insulator wafer (SOI) is firstly patterned to form waveguides. A III-V wafer is then bonded to the SOI wafer, polished to leave only the active region, and then lithographically patterned [21-22]. In another case, a III-V gain block is placed into an engineered pit on the SOI wafer, then patterned and metallized to form a laser [23]. Lasers integrated this way do not suffer from the defect issue of monolithic lasers, and maintains some key advantages of monolithic devices, such as lithographically defined connections. There are also apparent drawbacks. For example, III-V and SOI wafers are mis-matched in size, with SOI wafers being 8 or 12 inch diameter and III-V wafer usually only 2 to 3 inch diameter. The most significant roadblock to a practical application of this type of devices is that they involve III-V materials and processing, which raise serious concern in a CMOS fab.

1.4.4 Hybrid laser integration by edge coupling RSOA

The third approach is hybrid integration. A reflective semiconductor optical amplifier (RSOA) is edge coupled to a silicon photonics chip to form an external cavity laser [24-25]. In this case, mature III-V RSOAs can be utilized. The RSOA and silicon chip are independent and can be optimized separately. Micron scale alignment

is required in this case. But state-of the-art optoelectronics packaging tools can be used for the alignment. For example, it has been demonstrated that flip-chip bonders can do the alignment with sufficient accuracy. As a result, this is the most promising solution for near to mid future applications.

1.4.5 Laser cavity on silicon

Since all of these gain integration approaches involve having at least part of the laser cavity on the silicon chip, the silicon laser cavity design is also critical to the device performance. The cavity waveguide is relatively simple, so the wavelength selective mirror at the end of the cavity is key. Conventional Distributed Bragg reflectors (DBR) achieve the required functionality, so cavity designers considered them first. However, with the high index contrast and submicron waveguide widths mentioned before, grating sizes on a silicon waveguide needs to be sub-100 nm [28], which is beyond the process resolution of main stream silicon photonics processes. Since micro ring filters are generally available in silicon photonics platforms, the problem can be reduced to an on-chip broadband partially reflective mirror, which can be further decoupled into a 100% reflective mirror in series with a directional coupler to tap out a desired percentage of the cavity circulating power. The 100% reflective mirror could be implemented by tying up the two branches of a 3 dB Y-junction power splitter. In this design, the partial reflective mirror consists of only common and reliable components from the device library. However, a mirror built this way has two output ports from the directional coupler. Because there is no straightforward phase relationship between these two outputs, they are challenging to combine. If the laser doesn't happen to be the source for a parallel transmitter, output from one port will be

wasted. A reliable laser cavity configuration that suits the silicon photonics platform remains elusive in the literature.

Chapter 2 covers the basic principles of passive devices of silicon photonic integrated circuits, including Maxwell's equations, mode solving, mode overlap integral, finite difference time domain (FDTD) method, and particle swarm optimization (PSO). Since the silicon portion of a hybrid laser cavity is essentially a passive device (apart from the thermal tuning and control elements), these principles serves for some of the theoretical background of laser cavity design. The methodology of using FDTD coupled with PSO is illustrated with the design of a compact and low-loss Y-junction. Then the design of a high-efficiency germanium-assisted grating coupler is presented. The germanium is epitaxially grown in the same step as for building photodetectors, so no extra fabrication step is required. Coupling efficiency is 76% at 1.55 μm based on FDTD simulation, with over 40 nm 1 dB optical bandwidth.

In Chapter 3, I demonstrate a single adiabatic microring-based external cavity laser using reflective SOA and a silicon photonics chip. The laser operated at 1570 nm, and was measured to have 9.8 mW on-chip output power, less than 220 kHz linewidth, and over 45 dB side-mode suppression ratio. To make it easier to adjust the reflectivity of the on-chip partially reflective mirror, a Sagnac-loop based laser cavity is proposed and characterized. A laser using a Sagnac-loop mirror is also presented working at 1302 nm for O-Band applications. Sagnac loop mirror was utilized in the O-Band device. Open eye diagrams at 10 and 40 Gb/s are demonstrated. In both devices, a microring resonator is used as an intra cavity wavelength filter, whose resonant wavelength shifts as temperature varies. I show a resonant wavelength

stabilization approach based on a band-gap temperature sensor and active feedback control to conclude this Chapter.

In Chapter 4, a multi-wavelength laser is demonstrated. Ring resonators in silicon photonics offer a compact device footprint, low energy consumption, and inherent wavelength division multiplexing (WDM) capability. High performance ring modulators, wavelength filters and multiplexers have all been demonstrated, while a multi-wavelength laser source remains elusive to complete the system. The multi-wavelength external cavity laser consists of a quantum dot (QD) RSOA and a silicon photonics chip. QD RSOA offers less mode partition noise than conventional bulk or quantum well gain medium due to strong spectral whole burning. The silicon photonics chip provides a partially reflective mirror with multiple pass bands. Four lasing peaks with less than 3 dB power non-uniformity were measured, and error free 4×10 Gb/s data transmission using the multi-wavelength laser as the light source was demonstrated.

REFERENCES

1. R. Soref, “The past, present, and future of silicon photonics,” IEEE J. Sel. Topics Quantum Electron. 12(6), 1678-1687 (2006).
2. D. Liang and J. E. Bowers, “Recent progress in lasers on silicon,” Nat. Photonics. 4(8), 511–517 (2010).
3. G. T. Reed, G. Mashanovich, F. Y. Gardes, and D. J. Thomson, “Silicon optical modulators,” Nat. Photonics 4, 518-526 (2010).
4. J. Michel, J. F. Liu, and L. C. Kimerling “High-performance Ge-on-Si photodetectors,” Nat. Photonics 4, 527-534 (2010).
5. M. Hochberg, N. Harris, R. Ding, Y. Zhang, A. Novack, Z. Xuan, and T. Baehr-Jones, “Silicon photonics: the next fabless semiconductor industry,” IEEE Solid State Circuits Mag. 5, 48-58 (2013).
6. B. Analui, D. Guckenberger, D. Kucharski, and A. Narasimha, “A fully integrated 20-Gb/s optoelectronic transceiver implemented in a standard 0.13-μm CMOS SOI technology,” IEEE J. Solid-State Circuits 41(12), 2945-2955 (2006).
7. B. G. Lee, A. V. Rylyakov, W. M. J. Green, S. Assefa, C. W. Baks, R. Rimolo-Donadio, D. M. Kuchta, M. H. Khater, T. Barwicz, C. Reinholm, E. Kiewra, S. M. Shank, C. L. Schow, and Y. A. Vlasov, “Monolithic silicon integration of scaled photonic switch fabrics, CMOS logic, and device driver circuits,” J. Lightw. Technol. 32(4), 743-751 (2014).
8. C. R. Doerr, L. Chen, D. Vermeulen, T. Nielsen, S. Azemati, S. Stulz, G. McBrien, X.-M. Xu, B. Mikkelsen, M. Givehchi, C. Rasmussen, and S. Y. Park, “Single-chip silicon photonics 100-Gb/s coherent transceiver,” in Optical Fiber Communication Conference, paper Th5C.1 (2014).

9. K. K. Lee, D. R. Lim, L. C. Kimerling, J. Shin, and F. Cerrina, “Fabrication of ultralow-loss Si/SiO2 waveguides by roughness reduction,” Opt. Letters 26(23), 1888-1890 (2001).
10. G. Li, et al, “Ultralow-loss, high-density SOI optical waveguide routing for macrochip interconnects,” Opt. Express 20(11), 12035-12039 (2012).
11. A. P. Knights, J. D. Bradley, S. H. Gou, and P. E. Jessop, “Silicon-on-insulator waveguide photodetector with self-ion-implantation engineered-enhanced infrared response,” J. Vac. Sci. Technol. A 24(3), 783–786 (2006).
12. T. Yin, R. Cohen, M. M. Morse, G. Sarid, Y. Chetrit, D. Rubin, and M. J. Paniccia, "31GHz Ge n-i-p waveguide photodetectors on silicon-on-insulator substrate," Opt. Express 15(21), 13965-13971 (2007).
13. L. Vivien, J. Osmond, J.-M.c Fédéli, D. Marris-Morini, P. Crozat, J.-F. Damlencourt, E. Cassan, Y.Lecunff, S. Laval, "42 GHz p.i.n germanium photodetector integrated in a silicon-on-insulator waveguide," Opt. Express 17(8), 6252-6257 (2009).
14. S. Liao, N.-N. Feng, D. Feng, P. Dong, R. Shafiiha, C.-C. Kung, H. Liang, W. Qian, Y. Liu, J. Fong, J. E. Cunningham, Y. Luo, and M. Asghari, "36 GHz submicron silicon waveguide germanium photodetector," Opt. Express 19(11), (2011).
15. G. Li, Y. Luo, X. Zheng, G. Masini, A. Mekis, S. Sahni, H. Thacker, J. Yao, I. Shubin, K. Raj, J. E. Cunningham, and A. V. Krishnamoorthy, "Improving CMOS-compatible germanium photodetectors," Opt. Express 20(24), 26345-26350 (2012).
16. Y. Zhang, S. Yang, Y. Yang, M. Gould, N. Ophir, A. E.-J. Lim, G.-Q. Lo, P. Magill, K. Bergman, T. Baehr-Jones, and M. Hochberg, “A high-responsivity photodetector absent metal-germanium direct contact,” Opt. Express 22(9), 11367-11375 (2014).
17. H. Rong et al, “A continuous-wave Raman silicon laser,” Nature 433, 725-728 (2005).

18. T. J. Kippenberg, “Demonstration of an erbium-doped microdisk laser on a silicon chip,” Phys. Rev. A 71, 051802R (2006)
19. R. E. Camacho-Aguilera, Y. Cai, N. Patel, J. T. Bessette, M. Romagnoli, L. C. Kimerling, and J. Michel, “An electrically pumped germanium laser,” Opt. Express 20(10), 11316-11320 (2012).
20. T. Wang, H. Liu, A. Lee, F. Pozzi, and A. Seeds, "1.3-μm InAs/GaAs quantum-dot lasers monolithically grown on Si substrates," Opt. Express 19(12), 11381-11386 (2011).
21. A. W. Fang, R. Jones, H. Park, O. Cohen, O. Raday, M. J. Paniccia, and J. E. Bowers, "Integrated AlGaInAs-silicon evanescent racetrack laser and photodetector," Opt. Express 15(5), 2315-2322 (2007).
22. S. Keyvaninia, G. Roelkens, D. V. Thourhout, C. Jany, M. Lamponi, A. L. Liepvre, F. Lelarge, D. Make, G.-H. Duan, D. Bordel, and J.-M. Fedeli, “Demonstration of a heterogeneously integrated III-V/SOI single wavelength tunable laser,” Opt. Express 21(3), 3784-3792 (2012).
23. T. Creazzo, E. Marchena, S. B. Krasulick, P. Yu, D. Van Orden, J. Y. Spann, C. C. Blivin, L. He, H. Cai, J. M. Dallesasse, R. J. Stone, and A. Mizrahi, "Integrated tunable CMOS laser," Opt. Express 21(23), 28048-28053 (2013).
24. A. J. Zilkie, P. Seddighian, B. J. Bijlani, W. Qian, D. C. Lee, S. Fathololoumi, J. Fong, R. Shafiiha, D. Feng, B. J. Luff, X. Zheng, J. E. Cunningham, A. V. Krishnamoorthy, and M. Asghari, “Power-efficient III-V/Silicon external cavity DBR lasers,” Opt. Express 20(21), 23456-23462 (2012).
25. S. Tanaka, S-H Jeong, S. Sekiguchi, T. Kurahashi, Y. Tanaka, and K. Morito, “High-output-power, single-wavelength silicon hybrid laser using precise flip-chip bonding technology,” Opt. Express 20(27), 28057-28069 (2012).
26. J. W. Jenkins, J. D. Dow, “Electronic properties of metastable $Ge_{1-x}Sn_x$ alloys,” Phys. Rev. B, 36, 7994-8000 (1987)
27. G. He, H. A. Atwater, “Interband transitions in SnxGe1-x alloys,” Phys. Rev. Lett., 79, 1937- 1940 (1997)

28. X. Wang, W. Shi, H. Yun, S. Grist, N. A. F. Jaeger, L. Chrostowski, "Narrow-band waveguide Bragg gratings on SOI wafers with CMOS-compatible fabrication process", Opt. Express 20(14), 15547-15558 (2012)

Chapter 2

PASSIVE DEVICES DEISIGN AND OPTIMIZATION

Basic principles of passive devices of silicon photonic integrated circuits, including Maxwell's equations, mode solving, and mode overlap integral, are reviewed in Section 2.1. A numerical design method via a combination of finite difference time domain (FDTD) and particle swarm optimization (PSO) is then introduced, together with a Y junction design example. I helped design and characterize a number of passive devices, such Y-junctions, waveguide crossings, multimode interference (MMI) couplers etc. Through this process I learned passive device design methodology and characterization procedures. Equipped with such knowledge, I came up with the idea of using germanium to improve the efficiency of grating couplers. The germanium is grown in the same step for fabricating photodetectors, so no extra processing is required. In Section 2.2, a germanium-assisted grating coupler design with 76% coupling efficiency and 40 nm 1 dB bandwidth is proposed and verified by FDTD and PSO simulation.

2.1 Principles and Design Methodology

Propagation of electromagnetic wave in a dielectric medium is governed by Maxwell's equations 2.1-2.2.

$$\nabla \times \vec{H} = -\mu \frac{\partial \vec{E}}{\partial t} \tag{2.1}$$

$$\nabla \times \vec{H} = \varepsilon \frac{\partial \vec{E}}{\partial t} \tag{2.2}$$

where $\mu=\mu_0\mu_r$ and $\varepsilon= \varepsilon_0\varepsilon_r$ are the permeability and permittivity of the medium respectively. For non-magneto medium, $\mu=\mu_0$, the permeability of vacuum. The refractive index of the material is $n = \sqrt{\mu_r \varepsilon_r}$.

2.1.1 Finite difference time domain method

To predict the electromagnetic response of a complex device geometry, Maxwell's equation in 2.1-2.2 needs to be solved numerically. For example, one typical need is to evaluate the insertion loss of a device. In integrated optics, where the device size is on the order of its operating wavelength, finite difference time domain (FDTD) is the common method to numerically solve Maxwell's equation. The vector equation 2.1 is firstly recast into scalar form,

$$-\mu \frac{\partial H_x}{\partial t} = \frac{\partial E_z}{\partial y} - \frac{\partial E_y}{\partial z} \tag{2.3}$$

$$-\mu \frac{\partial H_y}{\partial t} = \frac{\partial E_x}{\partial z} - \frac{\partial E_z}{\partial x} \tag{2.4}$$

$$\mu \frac{\partial H_z}{\partial t} = \frac{\partial E_x}{\partial y} - \frac{\partial E_y}{\partial x} \tag{2.5}$$

Eq. 2.2 can be treated in the same manner. Then the electromagnetic field as well as permittivity distribution is discretized based the Yee cell [1] in a Cartesian coordinate system.

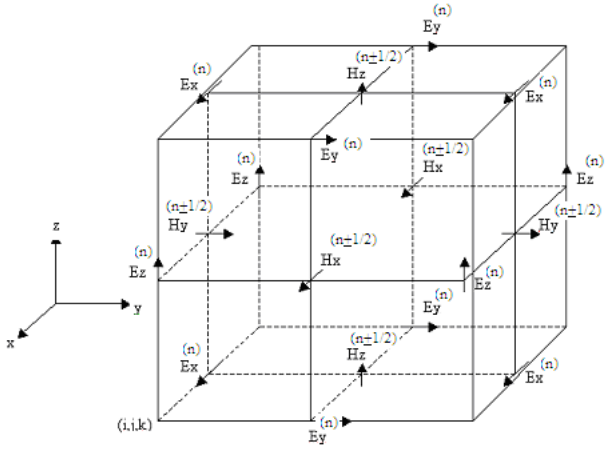

Figure 2.1 Yee cell, the unit cell used to numerically solve Maxwell's equations.

After discretization, the H-field at an arbitrary point can be calculate from its value at the previous time interval, and curl of E-field in the same cell as shown in Eq. 2.6 and Fig. 2.1, vice versa for E-field. In a single mode system, it is the fundamental mode of the waveguide that incidents on the input port. Since the insertion loss is the ratio of power at the output port to that at the input port, the absolute input power doesn't matter much in the simulation. Usually one assumes that a pulse in the fundamental mode with unit power incidents at the input port, and keeps doing the iteration described above until the pulse fully propagates through the device. The pulse at the output port can be captured, thus, the device insertion loss can be calculated.

$$\mu \frac{H_x^{n+\frac{1}{2}}(i,j+\frac{1}{2},k+\frac{1}{2}) - H_x^{n-\frac{1}{2}}(i,j+\frac{1}{2},k+\frac{1}{2})}{\Delta t} =$$

$$= \frac{E_y^n(i,j+\frac{1}{2},k+1) - E_y^n(i,j+\frac{1}{2},k)}{\Delta z} - \frac{E_z^n(i,j+\frac{1}{2},k+\frac{1}{2}) - E_z^n(i,j+\frac{1}{2},k+\frac{1}{2})}{\Delta y} \quad (2.6)$$

One quickly realizes that the fundamental mode needs to be obtained before starting the simulation. This is through a mode solver routine instead of the FDTD iteration. Substituting Eq. 2.2 into 2.1, the Maxwell's equation can be rewritten in the following form,

$$\nabla \times \nabla \times E = -\mu\varepsilon\omega^2 E \tag{2.7}$$

where ω is the angular frequency. This is an eigenvalue problem, and the eigenvector gives the E-field mode profile.

We also note that the ratio of the captured power at the output port to the launched power at the input port is not necessarily the device insertion loss. It is possible that higher order modes are excited in the device, thus the captured power at the output port is distributed in a number of modes. In a single mode system, high order modes gradually leak out while propagating down the waveguide. Hence the power in the fundamental mode needs to be extracted to accurately calculate the insertion loss. This can be achieved by a mode overlap integral, as described in Eq. 2.8, where φ_0 is the fundamental mode profile, and Ψ is the field pattern captured at the output port.

$$P = \langle \varphi_0 | A | \Psi \rangle = \int dA \begin{pmatrix} E_{x0}^* & E_{y0}^* & E_{z0}^* & H_{x0}^* & H_{y0}^* & H_{z0}^* \end{pmatrix} \begin{pmatrix} 0 & 0 & 0 & 0 & 1 & 0 \\ 0 & 0 & 0 & -1 & 0 & 0 \\ 0 & 0 & 0 & 0 & 0 & 0 \\ 0 & -1 & 0 & 0 & 0 & 0 \\ 1 & 0 & 0 & 0 & 0 & 0 \\ 0 & 0 & 0 & 0 & 0 & 0 \end{pmatrix} \begin{pmatrix} Ex \\ Ey \\ Ez \\ Hx \\ Hy \\ Hz \end{pmatrix} \tag{2.8}$$

The basic principles of integrated optical device, including Maxwell's equations, FDTD, mode solving and mode overlap integral is summarized. Although there are commercial software packages that implement the algorithms and equations above, it is still very beneficial to learn the basic principles to fully understand the

settings and properly interpret the result. Another issue that is common in almost all numerical simulation is the mesh accuracy. An ultrafine mesh generates accurate results, but is also extremely computationally expensive. Although a rough mesh is fast to run, the result might be less accurate. Usually the designer starts with a relatively rough mesh to double check the simulation settings as well as qualitatively check the simulation result, then gradually increase the mesh density until the result converges.

2.1.2 Particle swarm optimization

With the FDTD method described in the previous section, electromagnetic response of an arbitrary geometry can be accurately modeled. In other words, for any given device geometry, we can evaluate its properties such as insertion loss, wavelength or polarization dependence. However, it is unclear how to come up with a high performance device design just with FDTD. The manual trial and error method is too inefficient for practical applications. Hence there is a need to have some optimization method to couple with FDTD to address this design challenge. Basically the optimization algorithm generates multiple device variants, next FDTD will evaluate the performance of each variant, and then the optimization algorithm generates the second generation of device variants based on feedback from FDTD. The optimization process continues until a satisfactory device emerges.

Particle swarm optimization (PSO) was initially inspired by social behavior of swarm of bees, flocks of birds, or schools of finishes [2]. Taking the example of bee swarming, a bee will inspect a site, return to the swarm and send a message. A second bee will keep trying new sites or visit the site based on the message from the first bee. Either way, the second bee provides feedback to the hive on the conclusion of its

adventure, whether it is a good, average, or poor site. The favorite sites get more visitors by compounding emphasis, thus increasing further visitors. Gradually the whole swarm head to the favorite site with highest flower density.

$$x_n = x_n + \Delta t * v_n \tag{2.9}$$

$$v_n = \omega * v_n + c_1 * rand() * (P_{best,n} - x_n) + c_2 * rand() * (g_{best,n} - x_n) \tag{2.10}$$

The behavior of bees can be described mathematically by Eq. 2.9-2.10. The n^{th} bee flies at velocity v_n and passes position x_n, which updates every time interval Δt. A bee has three types of intentions to adjust its velocity. First, it is inertial and wants to keep the old velocity. Secondly it wants to go back the best site in its own memory. Finally, it receives messages from other bees in the swarm and tends to visit the favorite site known by the whole group. The relative strength of these three intentions are scaled by three constants, w, c_1, and c_2. Due to the nature of insects, their behavior is not totally predictable; so two random numbers are added in the second and third term in Eq. 2.10.

2.1.3 FDTD-PSO design example

The device we used to testify the capability of the PSO – FDTD design methodology is a Y junction 3 dB power splitter. Due to the finite processing resolution of mainstream silicon photonics processes, sharp corners will round out. Thus a conventional Y junction consists of two circular waveguides have about 1.2 dB excess loss in addition to the 3 dB intrinsic splitter loss.

Our goal was to design a compact, low loss and wavelength insensitive Y-junction for submicron silicon waveguide, compatible with typical CMOS photonic processes, where 193 nm or 248 nm steppers are commonly used. A minimum feature

size of 200 nm was assumed during the design, which would not break the designs rules, thus ensuring optimal yield. Silicon waveguide geometry is 500 nm wide and 220 nm high and the taper width is 0.5 μm at the input and 1.2 μm at the output, as shown in Fig. 2.2(a). The length of the taper connecting input and output waveguides was set to 2 μm to keep the device compact. The taper was first digitalized into 13 segments of equal length. The width of each segment, labeled as *w1* to *w13* in Fig. 2.2(a), was optimized to achieve low loss coupling. Taper geometry is defined by spline interpolation of these 13 points. The optimization figure of merit (FOM) was the power in the TE_0 mode at either branch. It was calculated by the overlap integral of the TE_0 mode of a 500 nm × 220 nm waveguide with the detected field at the output branch at wavelength 1550 nm. Maximizing the power effectively reduces the scattering and back-reflection. The swarm population was set to 30. 2D FDTD was used as an approximation of 3D FDTD for computing efficiency during optimization. A commercially available code was used [3]. Within 50 iterations, one solution with sub-0.2 dB insertion loss emerged, as shown in Table 2.1. Then 3D FDTD was run on this solution to double check the result with a mesh equal to 1/34 of the free space wavelength. The insertion loss was determined to be 0.13 dB. Scattering is negligible, as shown in the contour plot of electric field in Fig. 2.2(b). There is an interference pattern at the input end, indicating existence of very weak back-reflection.

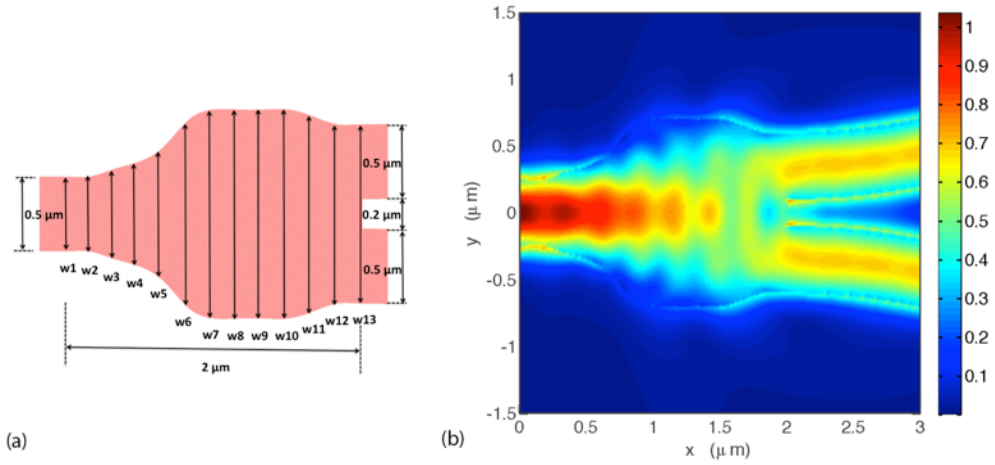

Figure 2.2 a) Schematic of device layout. The taper geometry is defined by spline interpolation of w1 to w13. b) Contour plot of simulated E-field distribution at 1550 nm wavelength.

Table 2.1. Taper width in µm

w1	w2	w3	w4	w5	w6	w7	w8	w9	w10	w11	w12	w13
0.5	0.5	0.6	0.7	0.9	1.26	1.4	1.4	1.4	1.4	1.31	1.2	1.2

The optimized device was prototyped by participating in a multi-project wafer (MPW) run offered by *OpSIS foundry*. Devices were measured on a wafer scale setup that can map the wafer coordinate to the stage coordinate, so that any device can be easily probed after initial alignment. Light from a tunable laser was coupled into the device under test (DUT) via a polarization maintaining (PM) fiber and grating coupler, then to a photodetector through another grating coupler and PM fiber.

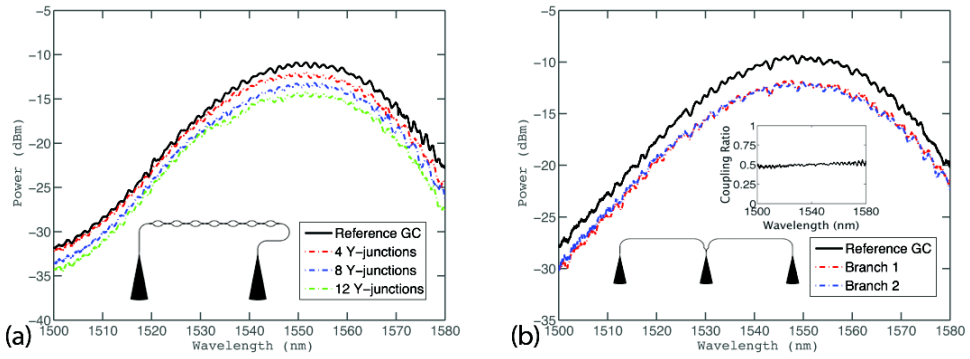

Figure 2.3 Typical measured spectra and corresponding test structure. The inset in (b) gives coupling ratio as a function of wavelength. Parabolic line shape and ripples are determined by grating coupler spectral response and imperfect linear polarization, respectively, as discussed in the main text. Offset in y-axis is from Y-junction insertion loss.

Typical measured spectra and corresponding test structure are shown in Fig. 2.3. The parabolic-like shape is determined by the grating coupler spectral response. For each transmission spectrum, a 30 nm wavelength span near the peak was fitted by a parabolic curve, and the maximum of the parabolic fit was used as the peak power in insertion loss calculation to minimize the effect of ripples. The measured peak power as a function of number of Y-junctions is plotted in Fig. 2.4(a). Blue dots are test data, and red line is a linear fit. The slope of the line gives the insertion loss in dB per Y-junction, 0.27 ± 0.01 dB in the case of the DUT. If a higher resolution process is available and the gap between the two branches can be shrunk from 0.2 μm to 0.1 μm, the device insertion loss can be reduced to below 0.1 dB according to FDTD simulations.

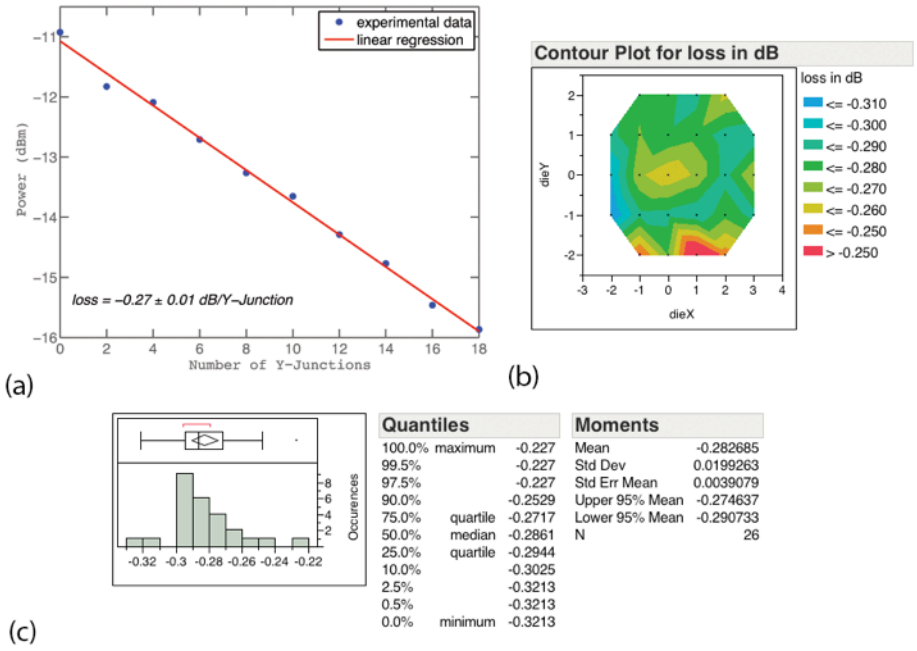

Figure 2.4 (a) Measured power as a function of the number of Y-junctions in the GC loop. Blue dots are measured peak optical power. Red line is linear fit; (b) Contour plot of measured Y-junction insertion loss across the wafer; and (c) Histogram of 26-reticle test data of measured insertion loss, showing mean value of 0.28 dB and standard deviation of 0.02 dB.

The testing results confirmed that the FDTD-PSO design method generated a compact, efficient and robust Y-junction. The same design methodology applies to other devices as well. I briefly mention a waveguide crossing here as another example. As the number of devices per chip increases, the complexity for device interconnects scales up quickly. A low loss, low cross talk and robust waveguide crossing significantly helps layout of complicated devices or systems, such as a 90 degree optical hybrid in a coherent receiver. In free space, two optical beams don't interfere even if they directly intersect. This is still true on chip, where to waveguides can cross and still maintain their optical signal. But at the same time, due to the lack of guiding

at the intersection, the mode diverges, which causes over 1 dB insertion loss and -10 dB cross talk. In principle, it is possible to reduce insertion loss and cross talk by reducing the divergence using multi-mode interference. A dedicated number of modes with specific amplitude ratio and phase relationship needs to be created, which is challenging, if possible at all, using conventional design approach. To utilize the FDTD-PSO method, the waveguide crossing is decomposed into four identical tapers. Then the taper is digitalized into 10 sections, similar to what we do for the Y-junction, as shown in Fig. 2.5. Waveguide crossing designed this way was measured to have 0.017 ± 0.005 dB insertion loss and lower than -35 dB cross talk, further validating the capability of this design methodology [4-5].

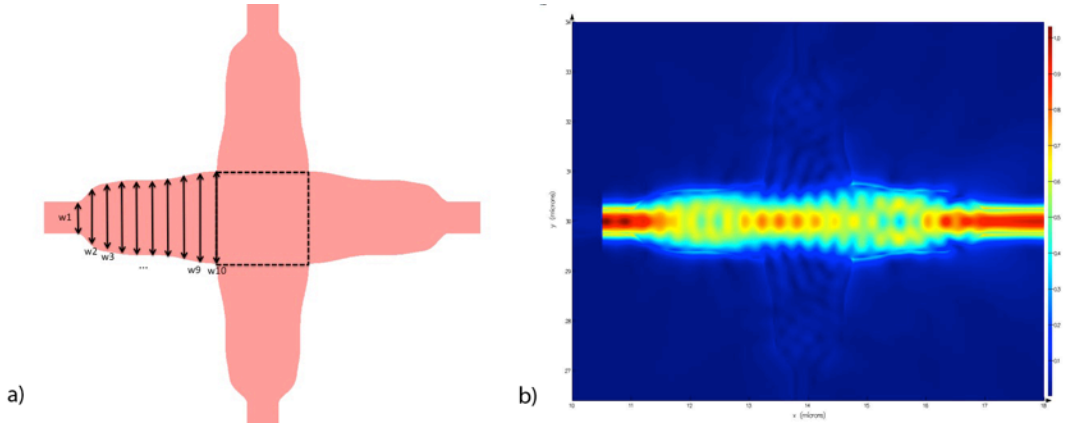

Figure 2.5 Optimized waveguide crossing: a) schematic and b) field pattern.

2.2 Germanium-assisted Grating Coupler

2.2.1 Grating coupler overview

Due to the large mode mismatch between submicron silicon waveguide and glass fiber, large coupling loss imposes a serious constraint on the power budget of

silicon based optical data links. An efficient fiber coupler has been a research focus for over a decade [6-7], and substantial progresses have been reported [8-18]. An inverse taper edge coupler can be used to expand the mode size by gradually decreasing confinement factor, thus reducing coupling loss [7-8]. Such edge couplers also have the advantage of low wavelength dependence. But they have to appear at the edge of the die and are only accessible after wafers are diced. Polishing might be required to get optical quality facet. On the other hand, grating couplers (GC) can be placed anywhere on the wafer, and enable wafer-scale testing, which is critical for process design kit development and inline performance monitoring in high volume production [9-18].

Since the silicon layer is sandwiched between the buried oxide (BOX) of the silicon-on-insulator (SOI) wafer and top oxide cladding, the refractive index is symmetric beneath and above the grating. Hence an equal amount of scattered power goes up and down, and maximal coupling efficiency is less than 50% for fully etched gratings. GC directionality can be defined as the ratio of optical power scattered upwards for ease of discussion. As light propagates to the grating region, the optical power in silicon gets depleted exponentially for uniform gratings, which doesn't mismatch the Gaussian profile of standard single mode fibers and causes further insertion loss. As a result, the first fabricated standard grating couplers had a coupling efficiency of only 19% [6]. The mode mismatch can be mitigated by utilizing apodized gratings instead of uniform gratings [9, 11-13]. Various approaches on improving directionality have been reported, including adding bottom reflectors using either dielectric DBRs [11] or coated metal [14], or depositing dielectric layers, poly-silicon [9-10] or silicon nitride [15], on top of gratings. Grating couplers with some

particular enhanced features, such as low back reflection [16], wide bandwidth [17], and low polarization sensitivity [18] were also reported. A major drawback of approaches to break index symmetry in the literature is that either non-standard SOI wafer needs to be used, or the process complexity is increased, which will ultimately increase the cost of silicon based PICs.

Here I propose a highly efficient grating coupler with germanium to enhance directionality. The germanium is epitaxially grown in the same step for building photodetectors, so no additional processing is needed. From finite difference time domain (FDTD) simulation, coupling efficiency as high as 76 %, corresponding to 1.2 dB insertion loss, could be achieved, with 1 dB bandwidth over 40 nm.

2.2.2 Selective growth of germanium

Since silicon is transparent in the 1.3 μm – 1.6 μm window, epitaxial germanium is commonly used as the light absorbing material of photodetectors in the silicon photonics platform. Similar to silicon wet etch, which stops naturally at <111> facet due to a much slower etch rate, germanium growth rate also depends on crystal orientations. Growth rate in <311> is slower than <100>. Fig. 2.6 shows a scanning electron microscope (SEM) image of germanium selectively grown on an <100> SOI wafer. Due to the growth rate selectivity, a trapezoid mesa is formed, which could be described by Wolf construction model [19]. A sidewall angle of 25 degrees is observed, determined by the facets between <311> and <100>.

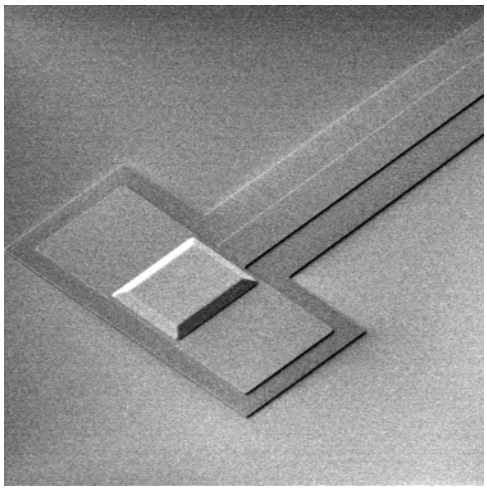

Figure 2.6 SEM image of Epi-Ge on an SOI wafer. Ge trapezoid base size is 8 μm x 11 μm. Unetched Si (220 nm thick) under Ge and partially etched Si (90 nm thick) surrounding unetched Si is also visible.

Germanium in detectors usually has height of between 500 nm and 800 nm, and width of a few microns. If the germanium strip width is narrower than 2 μm, two <311> facets intercept and a triangle the top will form. Recently, photodetectors without doping in germanium and metal-germanium direct contact based on this property of germanium growth were reported [20-21]. In the same epitaxy step, height of narrow germanium strips, between 200 nm and 250 nm wide, is expected to be about 200 nm, and can be fine-tuned by adjusting growth temperature, pressure and gas flow. With an absorption coefficient of 0.3 μm^{-1}, loss from absorption of 200 nm Ge is only 0.2 dB. On the other hand, the high real refractive index of Ge, 4.2, breaks symmetry of refractive index above and beneath silicon and significantly improves GC coupling efficiency.

2.2.3 Device layout and simulation

The device we proposed is shown in Fig. 2.7. The substrate is an SOI wafer with 220 nm single crystalline silicon film and 2 μm BOX on top of a silicon handle. A 60 nm partial etch is first applied to create the silicon grating, then 200 nm oxide hard mask is deposited, planarized, and patterned, followed by germanium epitaxy. Finally 2 μm oxide is also deposited as top cladding. This process is compatible and could be merged into with typical silicon photonics flow, such as the OpSIS-IME process.

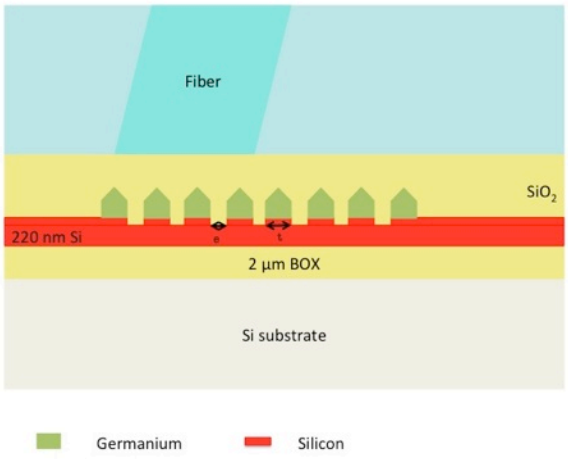

Figure 2.7 Schematic device cross-section

Germanium grating height is set to 230 nm, which is compatible with 500 nm to 800 nm thick Ge detectors in the same epitaxy step. Grating tooth and trench width are design variables. We performed FDTD simulations of the structure in Fig. 2.7 using a commercial software package [3]. Complex refractive index of Ge is used to

take both directionality improvement and light absorption into account. Light in TE0 mode is launched in the silicon waveguide, and propagates the grating region. Scattered light is monitored in a plane parallel to the wafer above the gratings. Coupling efficiency is determined by the overlap integral of the fiber mode and captured electromagnetic field profile. The smallest grating size was set to 80 nm, which is available in state-of-the-art silicon photonics processes [22-23]. 20 periods of gratings are used. To improve the mode overlap with standard single mode fiber, the strength of the first few gratings is kept low, and then grating tooth width is increased, and trench decreased, monotonically, optimized by PSO, as summarized in Table 1 and Table 2.

Table 2.2. Grating tooth width in nm.

t0	t1	t2	t3	t4	t5	t6	t7	t8	t9
80	80	80	84	91	98	105	112	119	126
t10	t11	t12	t13	t14	t15	t16	t17	t18	t19
133	140	147	154	160	160	160	160	160	160

Table 2.3. Grating trench width in nm.

e0	e1	e2	e3	e4	e5	e6	e7	e8	e9
616	616	616	616	616	610	602	594	586	578
e10	e11	e12	e13	e14	e15	e16	e17	e18	e19
570	562	554	546	538	530	522	514	506	498

The electric field pattern near the grating region without and with the germanium is plotted in Fig. 2.8. With the help of germanium grating, directionality increases by over a factor of two, from 39% to 92%, which is also visible in Fig. 2.8. Some interference pattern is also observed below the gratings, which is due to the reflection at BOX / silicon handle wafer interface.

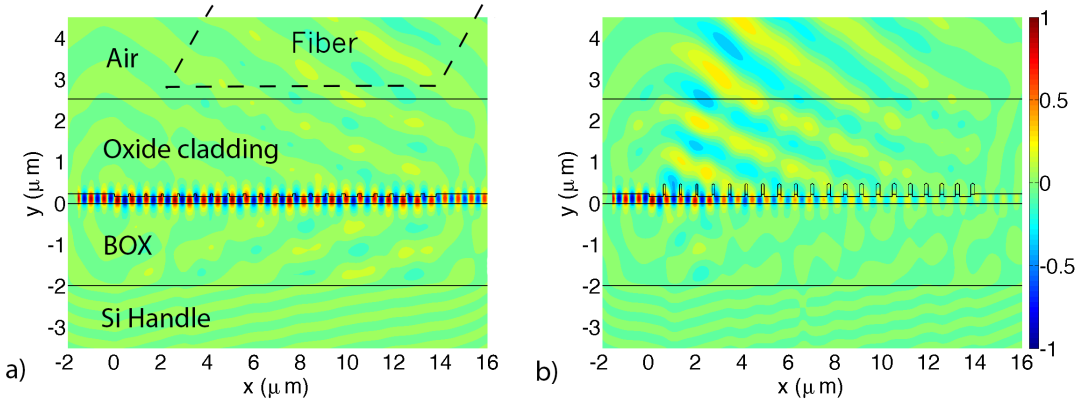

Figure 2.8 Electric field pattern near the grating region (a) without and (b)with germanium

Simulated grating coupler spectrum is shown in Fig. 2.9. The fiber angle was set to 19.5 degrees to tune the peak response to near 1.55 μm. At the optimal wavelength, coupling efficiency is 76%, or 1.2 dB, which is comparable to devices reported in the literature [7-16]. The 1 dB optical bandwidth is 40 nm, larger than the full C-Band telecom window.

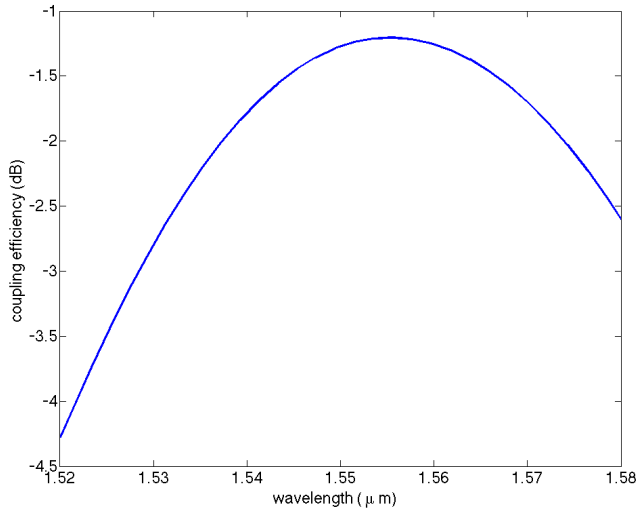

Figure 2.9 Grating coupler coupling efficiency as a function of wavelength.

We also examined the device fabrication sensitivity. Most sensitive geometry parameters are the slab layer thickness, depending on silicon partial etch depth, and the germanium grating height. The coupling efficiency when these two parameters are varied is plotted in Fig. 2.10. Within 10 nm processing non-uniformity, the coupling efficiency is drifts by 0.1 dB, which is acceptable in practical applications. The optimal grating height is near 230 nm, which provides optimal scattering strength, while keeping the absorption low. The coupling efficiency monotonically increases until the optimal slab thickness of 180 nm (not shown in Fig. 2.10). The slab layer thickness is set to 160 nm in the simulations, as this is typical value used and could be reliably fabricated.

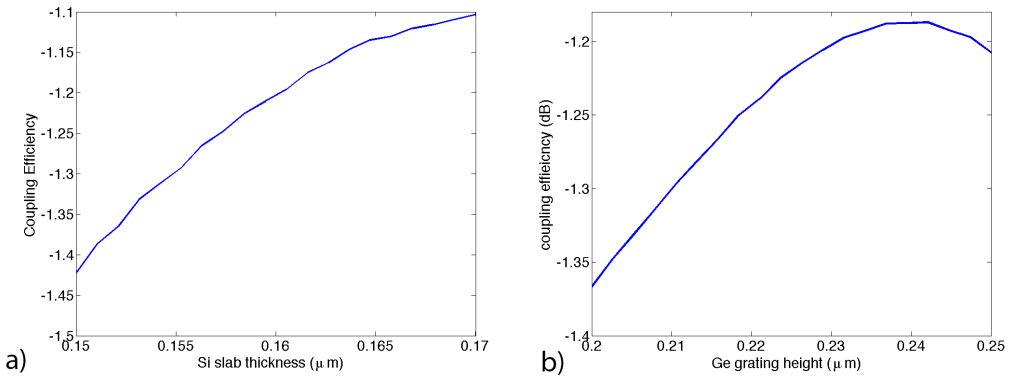

Figure 2.10 Coupling efficiency as a function of slab thickness and germanium grating height

2.3 Summary

Basic principles of passive devices of silicon photonic integrated circuits, including Maxwell's equations, mode solving, mode overlap integral, together with numerical method of FDTD and PSO, are reviewed, which serve as the foundation for on-chip laser cavity design in the rest of this thesis. The methodology of using FDTD coupled PSO is illustrated with the design of a compact and low loss Y junction. Then the design of a novel high efficiency germanium-assisted grating coupler is presented. The germanium is epitaxially grown in the same step for building photodetectors, so no extra fabrication step is required. Coupling efficiency is 76% at 1.55 μm based on FDTD simulation, with over 40 nm 1 dB optical bandwidth. This device is a building block for fiber to chip coupling of silicon photonics.

REFERENCES

1. K. S. Yee, "Numerical solution of initial boundary value problems involving Maxwell's equations in isotropic media," IEEE Trans. Antenas Propag. AP-14(3), 302-307 (1966).
2. J. Kennedy and R. Eberhart, "Particle swarm optimization," Proc. IEEE Intern. Conf. Neural Networks (1995).
3. http://www.lumerical.com/tcad-products/fdtd/.
4. Y. Zhang, S. Yang, A. E. Lim, G. Lo, C. Galland, T. Baehr-jones, and M. Hochberg, "A CMOS-Compatible,low-Loss, and low-crosstalk silicon waveguide crossing," IEEE Photon. Technol. Lett. 25(5), 422–425 (2013).
5. Y. Ma, Y. Zhang, S. Yang, A. Novack, R. Ding, A. E. Lim, G. Lo, C. Galland, T. Baehr-jones, and M. Hochberg,"Ultralow loss single layer submicron silicon waveguide crossing for SOI optical interconnect," Opt. Express 21(24), 29374-29382 (2013)
6. D. Taillaert, W. Bogaerts, P. Bienstman, T. F. Krauss, P.r Van Daele, I. Moerman, S. Verstuyft, K. De Mesel, and R. Baets, "An out-of-plane grating coupler for efficient butt-coupling between compact planar waveguides and single-mode fibers," IEEE J. Quantum Electron. 38(7), 949-955 (2002).
7. V. R. Almeida, R. R. Panepucci, and M. Lipson, "Nanotaper for compact mode conversion," Opt. Lett. 28(15), 1302-1304 (2003).
8. B. Ben Bakir, A. Vazquez de Gyves, R. Orobtchouk, P. Lyan, C. Porzier, A. Roman, and J.-M. Fedeli, "Low-loss (< 1 dB) and polarization-insensitive edge

fiber couplers fabricated on 200-mm silicon-on-insulator wafers," IEEE Photon. Technol. Lett. 22(11), 739-741 (2010).

9. G. Roelkens, D. Van Thourhout, and R. Baets, "High efficiency Silicon-on-Insulator grating coupler based on a poly-Silicon overlay," Opt. Express 14(24), 11622-11630 (2006).
10. D. Vermeulen, S. Selvaraja, P. Verheyen, G. Lepage, W. Bogaerts, P. Absil, D. Van Thourhout, and G. Roelkens, "High-efficiency fiber-to-chip grating couplers realized using an advanced CMOS-compatible Silicon-On-Insulator platform," Opt. Express 18(17), 18278-18283 (2010).
11. A. Mekis, S. Gloeckner, G. Masini, A. Narasimha, T. Pinguet, S. Sahni, and P. De Dobbelaere, "A grating-coupler-enabled CMOS photonics platform," IEEE J. Sel. Top. Quantum. Electron. 17(3), 597-608 (2011).
12. L. He, Y. Liu, C. Galland, A.E.-J. Lim, G.-Q. Lo, T. Baehr-Jones, and M. Hochberg, "A high-efficiency nonuniform grating coupler realized with 248-nm optical lithography," IEEE Photon. Technol. Lett. 25(14), 1358-1361 (2013).
13. A. Li, H. Zhang, M. Yu, and G. Q. Lo, "CMOS-compatible high efficiency double-etched apodized waveguide grating coupler," Opt. Express 21(7), 7868-7874 (2013).
14. W. S. Zaoui, A. Kunze, W. Vogel, M. Berroth, J. Butschke, F. Letzkus, and J. Burghartz, "Bridging the gap between optical fibers and silicon photonic integrated circuits," Opt. Express 22(2), 1277-1286 (2014).

15. W. D. Sacher, Y. Huang, L. Ding, B. J. F. Taylor, H. Jayatilleka, G.-Q. Lo, and J. K. S. Poon, "Wide bandwidth and high coupling efficiency Si3N4-on-SOI dual-level grating coupler," Opt. Express 22(9), 10938-10947 (2014).
16. Y. Wang, X. Wang, J. Flueckiger, H. Yun, W. Shi, R. Bojko, N. A. F. Jaeger, and L. Chrostowski, "Focusing sub-wavelength grating couplers with low back reflections for rapid prototyping of silicon photonic circuits," Opt. Express 22(17), 20652-20662 (2014).
17. Q. Zhong, V. Veerasubramanian, Y. Wang, W. Shi, D. Patel, S. Ghosh, A. Samani, L. Chrostowski, R. Bojko, and D. V. Plant, "Focusing-curved subwavelength grating couplers for ultra-broadband silicon photonics optical interfaces," Opt. Express 22(15), 18224-18231 (2014).
18. L. Carroll, D. Gerace, I. Cristiani, and L. C. Andreani, "Optimizing polarization-diversity couplers for Si-photonics: reaching the -1dB coupling efficiency threshold," Opt. Express 22(12), 14769-14781 (2014).
19. J. Liu, R. Camacho-Aguilera, J. T. Bessette, X. Sun, X. Wang, Y. Cai, L. C. Kimerling, and J. Michel, "Ge-on-Si optoelectronics", Thin Solid Films 520(8), 3354-3360 (2012).
20. T.-Y. Liow, N. Duan, A. E.-J. Lim, X. Tu, M. Yu, and G.-Q. Lo, "Waveguide Ge/Si Avalanche Photodetector with a Unique Low-Height-Profile Device Structure," Optical Fiber Communications Conference, Paper M2G.6 (2014).
21. Y. Zhang, S. Yang, Y. Yang, M. Gould, N. Ophir, A. E.-J. Lim, G.-Q. Lo, P. Magill, K. Bergman, T. Baehr-Jones, and M. Hochberg, "A high-responsivity photodetector absent metal-germanium direct contact," Opt. Express 22(9), 11367-11375 (2014).

22. E. Temporiti, G. Minoia, M. Repossi, D. Baldi, A. Ghilioni, and F. Svelto, “A 3D-Integrated 25Gbps silicon photonics receiver in PIC25G and 65nm CMOS technologies,” European Solid State Circuits Conference, 131-134 (2014).
23. S.-H. Jeong, D. Shimura, T. Simoyama, Mi. Seki, N. Yokoyama, M. Ohtsuka, K. Koshino, T. Horikawa, Y. Tanaka, and K. Morito, “Low-loss, flat-topped and spectrally uniform silicon-nanowire-based 5th-order CROW fabricated by ArF-immersion lithography process on a 300-mm SOI wafer,” Opt. Express 21(25), 30163-30174 (2013).

Chapter 3

HYBRID INTEGRATED LASER FOR SILICON PHOTONICS

An efficient electrically pumped laser source is one of the last few bottlenecks to overcome to complete the silicon photonics design kit. In Section 3.1-3.3, I present a laser based on the hybrid integration approach, as shown in Fig. 3.1. In 3.4, an O-Band version device is reported to address short reach communication applications. In addition to a different RSOA, I also adopted a silicon laser cavity design based on Sagnac loop mirror in the O-Band device for improved reliability. A microring resonator is used as intra-cavity wavelength filter in both devices. The resonant wavelength of the microring, thus the lasing wavelength, drifts as the temperature is changed. A wavelength stabilization approach based on band gap temperature sensor and closed loop feed back control is demonstrated in 3.5. I worked on the silicon device part, and my collaborators in Columbia University helped to implement the control circuit.

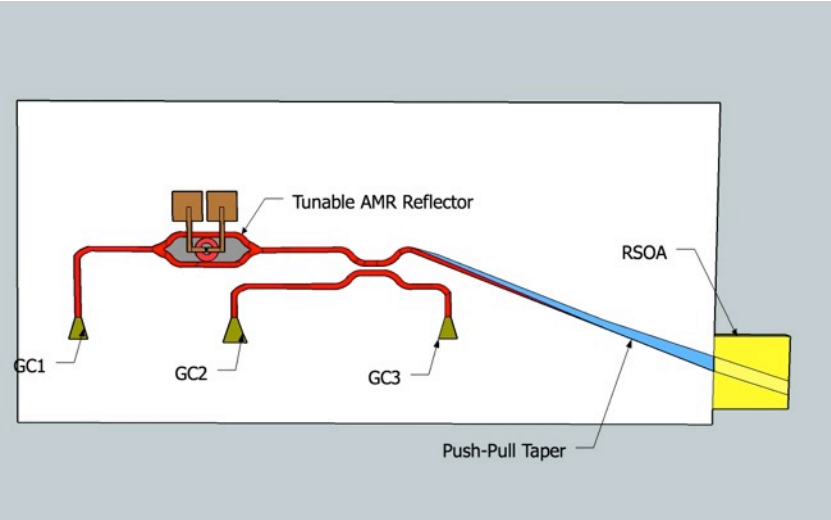

Figure 3.1 Isometric diagram of the layout of the laser system. The InP based RSOA is shown bonded to the SOI chip, which includes a tunable AMR reflector to close the laser cavity.

3.1 SOI Chip Design

The device consists of a commercially available InP-based RSOA (Thorlabs SAF 1126), and a SOI chip fabricated via the *OpSIS* multi-project wafer (MPW) foundry service to close the laser cavity. The SOI chip utilized a standard silicon-on-insulator (SOI) wafer with 220 nm thick top silicon film. The choice of a thin silicon layer makes for a higher level of compatibility with many currently utilized silicon photonics device geometries, but introduces a number of challenges. Compared to the hybrid laser in [1] which uses a SOI wafer with 3 μm top silicon, there is a large mode mismatch between submicron single mode silicon waveguide and the RSOA waveguide mode, introducing a performance-limiting coupling loss. A SiON or polymer spot size converter can be used on the silicon chip to match the RSOA mode, but this approach entails increased process complexity [2]. I used a novel ultra-thin

silicon edge coupler to achieve low loss coupling directly from partially-etched silicon, without the requirement of an additional layer.

A key challenge in the design of a hybrid III/V – silicon laser cavity is the need to introduce a reflector that can select a single mode from the high density of fundamental Fabry-Perot modes created in a relatively large cavity. Previous approaches have included either a distributed Bragg reflector (DBR) [1], or a combination of a ring resonator and a DBR [2], or a dual-ring [3, 4] or dual DBR [5] configuration that makes use of the Vernier effect. Using a single ring-resonator would be desirable, because it would simplify the system design. In [6, 7], the laser utilized a directional coupler to extract light from cavity, which resulted in two output ports with same power at the same wavelength. If used in a WDM transmitter, and the two output ports cannot be combined coherently, half of the output power will be wasted. We show that a laser using an adiabatic microring resonator (AMR) [8], can achieve attractive performance. The large free-spectral range (FSR) of the AMR enables the effective selection of a single lasing mode, without the need for a further frequency selection based on a second ring or a DBR. Fig. 3.1 shows a diagram of the hybrid system. The grating coupler (GC) on the left, GC1 in Fig. 3.1, is the on-chip laser output port, and where our power measurement is taken. In this case, a grating coupler has been attached to this port to enable us to measure the output power. GC2 and GC3 connect to a 10% directional coupler tap, serving as monitoring ports to help fully characterize the device. This allows the direct measurement of the internal power circulating in the cavity.

3.1.1 RSOA edge coupler

Efficient light coupling between a submicron silicon waveguide and an RSOA or laser diode has been challenging due to the large mode mismatch. The mode field diameter (MFD) of a single transverse mode semiconductor laser diode is usually a few microns in the horizontal direction and around 1 um in the vertical direction, while the dimension of typical SOI waveguide is only 500 nm x 220 nm, as shown in Fig. 3.2 (a) and (b). Adding a silicon nitride layer can help match the mode at the price of increased fabrication complexity. We adopt an alternative approach, and utilize a partially etched silicon layer. Most silicon photonics processes contain a partial etch step, usually in order to enable electrical contact in modulators. Here, we show that such a partial etch can provide a useful tool for mode-matching.

In the OpSIS-IME MPW platform, a 90 nm silicon thickness is available. It is possible to form a waveguide with much looser mode confinement with this geometry, as shown in Fig. 3.2 (c). The optical mode of the thin waveguide is larger in vertical direction and provides a significantly improved match to the RSOA waveguide mode. Theoretical coupling loss is simulated using finite-difference time-domain (FDTD) method. Coupling loss as a function of RSOA and silicon waveguide facet spacing is summarized in Fig. 3.3. State-of-the-art motored-controlled optical stages have a resolution better than 0.2 um. At such distance, insertion loss better than 1.9 dB can be achieved.

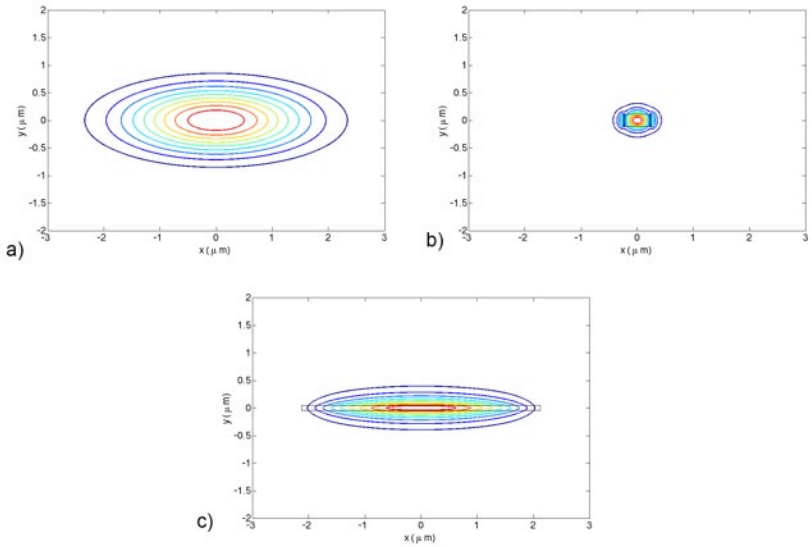

Figure 3.2 Mode Profiles (a) typical laser diode (b) 220 nm x 500 nm silicon waveguide (c) 90nm x 4.25 um silicon waveguide.

The thin waveguide width was first tapered from 4.25 μm to 1.2 μm over 150 μm, then a push-pull taper was used for transition between 1.2 μm x 0.09 μm waveguide and 0.5 μm x 0.22 μm routing waveguide [9]. The push-pull taper consists of two 150 μm overlapping tapers in opposing directions. To be consistent with the process design rules and minimize coupling loss, the 0.22 μm thick waveguide tapers from 0.5 μm to 0.18 μm, while the 0.09 μm thick waveguide tapers from 1.2 μm to 0.4 μm. The measured insertion loss of such push-pull taper is 0.8 dB from corresponding characterization structures.

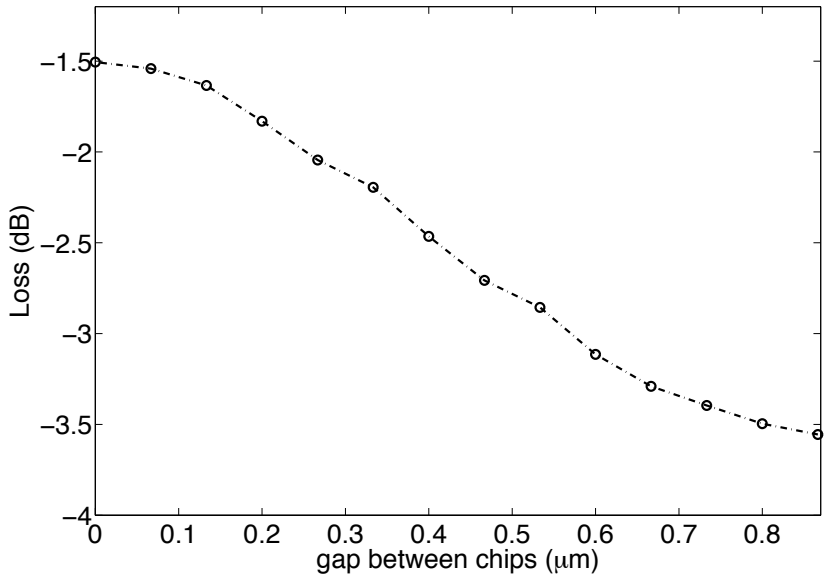

Figure 3.3 Loss as a function of the gap between the SOI chip and RSOA.

3.1.2 Inline reflector with adiabatic microring

Distributed Bragg reflectors (DBRs) are commonly used for narrow band reflection with large FSR values. Attractive DBRs made on SOI have been reported [10]. However, DBRs usually require high-resolution gratings and are very sensitive to fabrication variations. Inline reflectors appropriate for integrated lasers were proposed and demonstrated by Paloczi et al [11] and recently implemented in silicon [12]. These consisted of a ring or disk resonator incorporated in a Mach-Zehnder structure. Microring and disk resonators have been widely used for modulation, filtering and sensing in silicon photonics. One drawback of micro-rings is their sensitivity to fabrication variations. For wafers processed in a commercial CMOS fab, it has been reported that the cross-wafer spread in resonant wavelength is as large as its FSR [13]. If the micro-ring is used as a WDM modulator, the ring resonance can be thermally tuned to the nearest grid channel, thus mitigating the fabrication sensitivity to a certain

extent. However, if the micro-ring is used inside a laser cavity, the non-predictability of lasing wavelength greatly impedes the practical application of such device.

The effect of waveguide geometry variation on micro-ring resonance wavelength can be modeled as a perturbation to the waveguide effective index. The FSR depends on the group index of the waveguide, which is immune to fabrication errors and can be accurately controlled among wafers and lots [13]. If the FSR is increased to be significantly larger than the random spread of wavelengths, that spread determines the range of possible lasing wavelengths. The spread depends on ring waveguide design, the SOI wafer, and silicon processing. We chose an adiabatically widened micro-ring (AMR), which has a large FSR [14] and is more robust against fabrication variations [15]. In an AMR, waveguide is narrow near the coupling region to ensure single mode operation, and then gradually widened to support tight bend and possible need to form metal contact. For an AMR of 2 μm radius, the FSR is as large as 54 nm. As shown in Fig. 3.4(a), there is only one resonance peak in our testing laser's sweepable range,1500 nm to 1580 nm. Resonance FWHM is 1.38 nm, corresponding to a finesse of 39 or Q-factor of 1100. We measured the same device design on all 31 complete 2.5 cm × 3.2 cm reticles across an 8-inch wafer. Wafer chuck temperature was set to 30 °C, where it is most stable. The resonant wavelength distribution contours and statistics are shown in Figs. 3.4(b)-(c). The mean is 1528.76 nm and standard deviation is 3.32 nm.

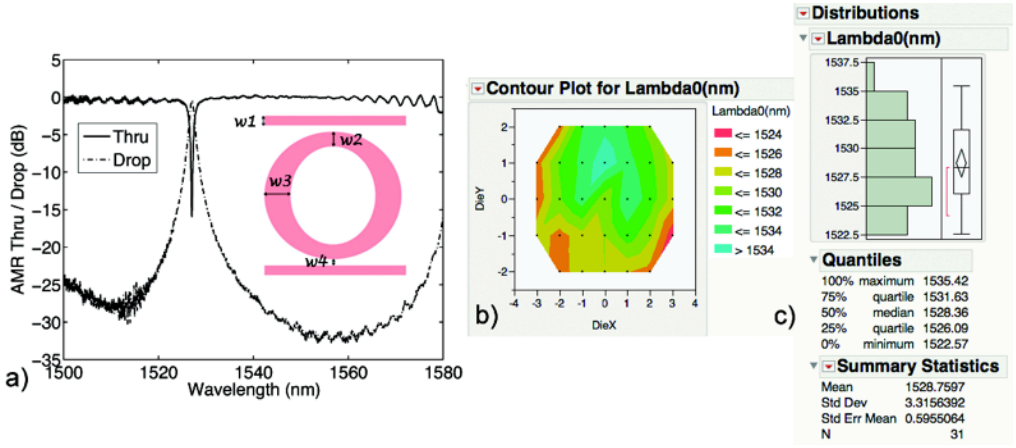

Figure 3.4 (a) Spectrum of AMR drop (solid) and through (dashed) ports. Inset is schematic of AMR layout, where w1 = 0.3 µm, w2 = 0.46 µm, w3 = 0.76 µm, and w4 = 0.2 µm; (b) Contour plot for resonant wavelength distribution across an 8-inch wafer; (c) Statistics of the resonant wavelength distribution.

To further validate the predictability of resonant wavelength, AMRs with slightly different radii on the same wafer were also measured, and summarized in Fig. 3.5 and Table 3.1. The wavelength range, maximum minus minimum, falls between 12.30 nm and 16.30 nm. Standard deviation is between 3.32 nm and 3.78 nm, with an average of 3.6 nm. Note that the device is patterned using 248 nm lithography on SOI wafers with 20 nm 3σ thickness variations. Significant device uniformity improvement was observed by switching to 193 nm [16], 193 nm immersion lithography, and more uniform wafers [17]. For WDM applications, the target wavelength can be set as the lower bound of the wavelength spread, and then locally and thermally tuned to the grid wavelength and stabilized with active feedback control [18]. Since the tuning range is a very small fraction of the FSR, thermal tuning power is minimal [19].

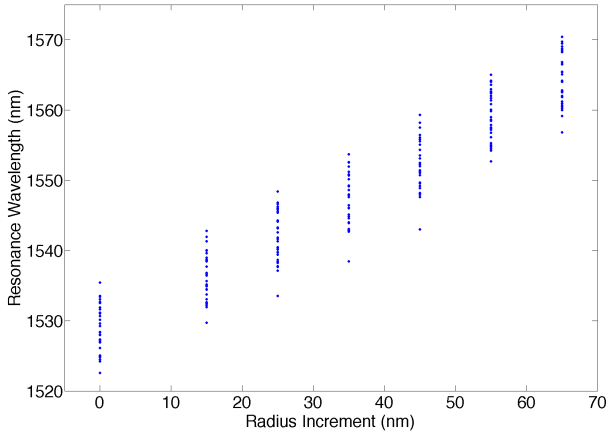

Figure 3.5 AMR resonance increase as ring radius increases, measured on 31 reticles across an 8-inch wafer.

Table 3.1. Resonant wavelength distribution of AMR with slightly different radius.

ΔR (nm)	0	15	25	35	45	55	65
Min	1522.57	1529.71	1533.52	1538.47	1543.00	1552.70	1556.80
Max	1535.42	1542.8	1548.42	1553.70	1559.30	1565.00	1570.41
Range	12.85	13.09	14.90	15.23	16.30	12.30	13.61
Std Dev.	3.32	3.38	3.59	3.75	3.78	3.47	3.62

In this work, an adiabatic ring based inline reflector is utilized to achieve narrowband reflection, as shown in Fig. 3.6. We increased the radius compared to 3 μm to make enough space to place metal vias inside the ring for the integrated thermal tuner. The transmission spectrum of the AMR based inline reflector is also plotted in Fig. 3.6, showing its FSR greater than 30 nm. The Q-factor of the loaded resonator is about 2550.

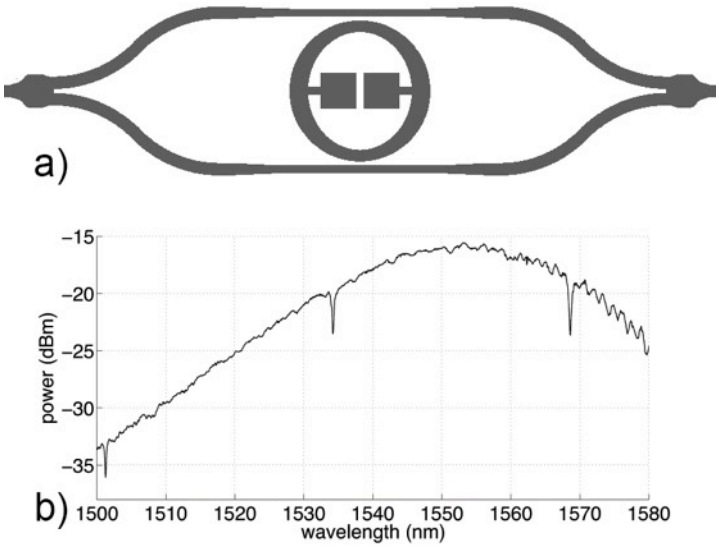

Figure 3.6 (a) AMR layout and (b) transmission spectrum.

The intrinsic Q value of the AMR has been degraded via coupling to the two waveguides and losses introduced by doping and metal vias. At the resonance peaks, there is thus preferentially more light reflected back into the laser cavity. The length of RSOA is 1 mm, and routing silicon waveguide before the AMR is about 1.35 mm, indicating the Fabry-Perot mode spacing is about 0.1 nm. Therefore, the overall cavity mode that lines up with this resonance peak will experience lasing.

3.2 Chip Alignment and Bonding

The SOI chip was fabricated by *Institute of Microelectronics* in Singapore via the *OpSIS* foundry service. Starting substrate was a standard 8-inch SOI wafer with 220 nm silicon film on top of 2 μm buried oxide (BOX). Three layers of lithography and etching were utilized to pattern the grating couplers, ultra-thin silicon edge coupler, and strip waveguides. Then dopants and metal interconnects were added to

make the AMR tunable, via the creation of an integrated heater inside the AMR. The RSOA (Thorlabs SAF 1126) is commercially available.

3.2.1 Test setup

An edge coupling set up was put together from scratch for testing and characterizing the external cavity laser. The setup consists of three sub systems for alignment, viewing and imaging, and temperature control. Two 6-axis stages from Newport are used for micron scale alignment accuracy. Some customized chip chucks were self-machined in the University machine shop. These chucks accomplish a few functions, including holding the chips by vacuum (together with an external pump), embedding a thermal electric cooler (TEC) for temperature control, and on the cold side of the TEC, there are tunnels for flowing coolant to take away the heat. Deionized water picked up from the cleanroom was used as coolant in this case.

Two sets of inspection scopes were used for viewing and imaging during the alignment. One with 12x was usually used for landing probes on the gain chip, bringing lensed fiber close to the far end facet of the gain chip, and rough alignment between the silicon chip and gain chip. Then the other inspection scope with 50x lens was switched in for fine alignment between the silicon and IIIV waveguide facets, as well as between lensed fiber and far end facet of the gain chip. Switching the two inspection scopes back and forth is sometimes needed, which needs to be done with great caution to minimize vibration. For the same reason, all wires and fibers are taped down to the optical table. It is also helpful sometimes to replace the visible camera with an infrared camera.

The last piece of the setup is a fiber array holder and controller. After the gain chip and silicon chip are properly aligned, a fiber array is used to probe the grating

couplers on the silicon chip to pick up the laser output power. In most cases, the on-chip output power is of interest, which can be back calculated by normalizing the grating coupler insertion loss.

3.2.2 Alignment procedure

The silicon chip was polished after wafer dicing to create a flat and smooth facet for butt coupling. No anti-reflective coating was applied on the silicon chip. Then both the RSOA and the silicon chip are mounted on six-axis stages for active alignment. The gain chip was kept at 25 C using a thermo-electric cooler (TEC), while the silicon chip was at the ambient temperature of the metal chuck. The RSOA and SOI chip were aligned to each other, and then the fiber array was aligned to grating couplers on the SOI chip, as shown in Fig. 3.7.

After both anode and cathode probes were in contact with corresponding metal pads on the RSOA, and pump current was flowing properly, a lensed fiber was brought near the high reflective end of the RSOA to monitor the cavity ASE or lasing condition as a feedback for the alignment. The silicon chip position was manually rastered until power in the lensed fiber is maximized. A big jump was observed when lasing started, and the power increased further as the silicon position was optimized. A bright spot at the output grating coupler was visible on an infrared camera at this step. We then turned off the laser pump current temporarily for grating coupler alignment. A fiber array was brought into proximity of the silicon chip surface to probe the grating coupler. The two pigtail fibers from the array are connected to an Agilent testing laser and power meter for active alignment. The fiber to chip coupling loss was determined to be 14 dB, which is less than optimal because we wanted to avoid perturbing the RSOA to silicon chip alignment. This can be improved in the future

when the gain chip is securely bonded. Once the fiber array was aligned, the Agilent laser was turned off, and the RSOA pump current for the device under test (DUT) was turned back on. Device characterization was performed under this condition.

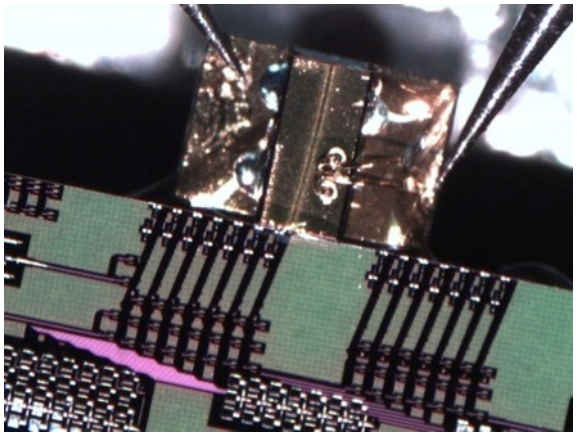

Figure 3.7 Test Setup image showing silicon photonic chip (bottom) and RSOA chip (top).

3.3 Hybrid Laser Characterization

3.3.1 Output power and coupling loss

The bonded chip was characterized using a fiber array to probe the output grating couplers, GC1 to GC3 in Fig. 3.1. The parallel waveguide length in the directional coupler between GC2 and GC3 is 5 um, and the separation between them is 200 nm, corresponding to 10% coupling ratio. GC1 is the main output port. GC2 and GC3 are laid out for monitoring purpose. The GC1 output is plotted in Fig. 3.8. An SMSR over 45 dB is observed. On-chip output power at the port coupled to GC1 is observed to be 9.8 mW when current is set to 320mA. Stage chuck temperature was set to 20 °C during the measurement. By comparing the power at all three GCs, the

transmittance and reflectivity of the inline reflector was found to be 29% and 0.4%, while 67% of light is lost, most likely because of metal absorption due to contacting the inner part of the ring. Cavity circulating power before the inline reflector is estimated to be 33.8 mW.

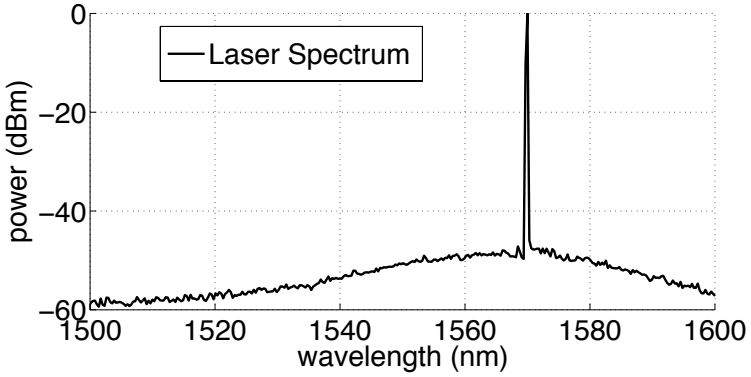

Figure 3.8 Spectrum of our Hybrid-integrated Laser.

The continuous wave (CW) light intensity as a function of pump current, L-I curve, is shown in Fig. 3.9. The L-I curve shows a threshold at around 60 mA, and slope efficiency of 42 mW/A. Optical probing of grating couplers GC2 and GC3 enables the transmission, reflection and insertion loss of the inline reflector can be characterized.

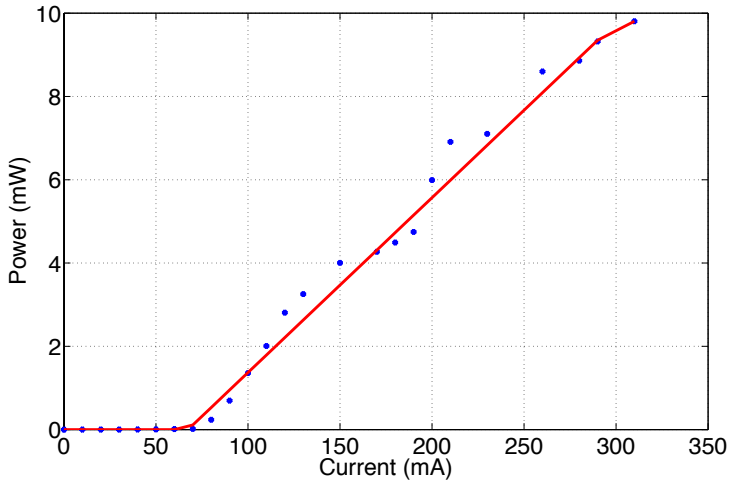

Figure 3.9 CW L-I curve showing a threshold current of around 60 mA and the red fitting curve shows a slope efficiency of 42 mW/A.

Based on the theory in [20], the slope efficiency of an external cavity laser depends on the effective mirror transmittance and reflectivity, as described in Eq. 3.1.

$$\frac{\Delta P}{\Delta I} = \frac{T_{eff}\sqrt{R_1}}{(1-R_{eff})\sqrt{R_1}+(1-R_1)\sqrt{R_{eff}}} \times \left(\frac{h\nu}{q}\frac{n_{ext,f}}{n_i}\right) \tag{3.1}$$

where n_i and n_{ext} are the internal and external quantum efficiency of the laser. The internal quantum efficiency measures the number of photons generated by injection of an electron. Above threshold, any injected electron yields a photon within the laser cavity, thus n_i should approach unity. The external quantum efficiency denotes the portion of generated photons that will actually leave the laser cavity. The ratio between the two is described in Eq. 3.2 below.

$$\frac{n_{ext,f}}{n_i} = \frac{\ln(1/R_1R_{eff})}{2\alpha_s L_D + \ln(1/R_1R_{eff})} \tag{3.2}$$

The effective transmittance and reflectivity lumps up coupling loss between silicon chip and gain chip, edge coupler insertion loss, directional coupler and mirror losses, as shown in Eq. 3.3-3.4.

$$T_{eff\_dB} = Coupling\_Loss + IL_{edge\_coupler} + L_{DC} + L_{reflector} \tag{3.3}$$

$$R_{eff\_dB} = 2 * (Coupling\_Loss + IL_{edge\_coupler} + L_{DC} + L_{reflector}) \tag{3.4}$$

The loss values are easier to sum up in logarithmic form, but needs to be converted back to decimal before substituting in Eq. 3.1-3.2, as shown below.

$$T_{eff} = 10^{(-T_{eff\_dB}/10)} \tag{3.5}$$

$$R_{eff} = 10^{(-R_{eff\_dB}/10)} \tag{3.6}$$

With R_1 being the reflectivity far end facet of the gain chip and slope efficiency of 42 mW/A measured in Fig. 3.7, the coupling loss was calculated to be 3.5 dB. This was higher than the 1.8 dB as we expected in 3.1.1, most likely due to a larger gap in our manual alignment.

3.3.2 Linewidth

The true line width cannot be determined from the spectrum in Fig. 3.6, as the measurement is limited by the optical spectrum analyzer (OSA) resolution to about 0.2 nm. We'll first estimate the linewidth of this laser using Heny's formula [21], Eq. 3.7,

$$\Delta\nu = \frac{v_g^2 h\nu n_{sp}(1+\alpha^2)}{8\pi P_0}(\alpha_m + \alpha_i)\alpha_m \tag{3.7}$$

where $h\nu$ is the photon energy, n_{sp} is the spontaneous emission coefficient, α is the linewidth enhancement factor, and P_0 is the laser output power. α_m and α_i are related to cavity length, coupling loss and mirror reflectivity, as shown in Eq. 3.8-3.9.

$$\alpha_m = \frac{1}{L_{SOA} + L_{filter}} \ln\left(\frac{1}{\sqrt{R_1 R_2}}\right) \tag{3.8}$$

$$\alpha_i = \frac{L_{SOA}\alpha_{SOA} + L_{filter}\alpha_{filter} + \delta_{coupling}}{L_{SOA} + L_{filter}} \tag{3.9}$$

Substituting typical SOA parameters, output power and coupling loss calculated above, the line width is calculated to be 110 kHz.

To measure the true linewidth, output of the hybrid laser was combined with output from a test laser (Agilent 81600B) using a fiber 3 dB coupler and the combined signal was fed into a photodetector (PD) to be converted to electrical domain. The PD RF output was monitored by a Tektronix RSA 6114A electrical spectrum analyzer (ESA) with resolution bandwidth (RBW) set at 100 kHz. The wavelength of Agilent laser was set to be very close to the silicon laser, with a difference within the bandwidth of the ESA. A diagram of this experiment and the measured spectrum is shown in Fig. 3.10 and Fig. 3.11. The Agilent laser is known to have a linewidth of 100 kHz. From the spectrum in Fig. 3.11, the combined Lorentzian linewidth is 220 kHz. This is a sufficiently narrow linewidth that our hybrid integrated laser can even be used in coherent communication systems, which have some of the narrowest linewidth requirements [26].

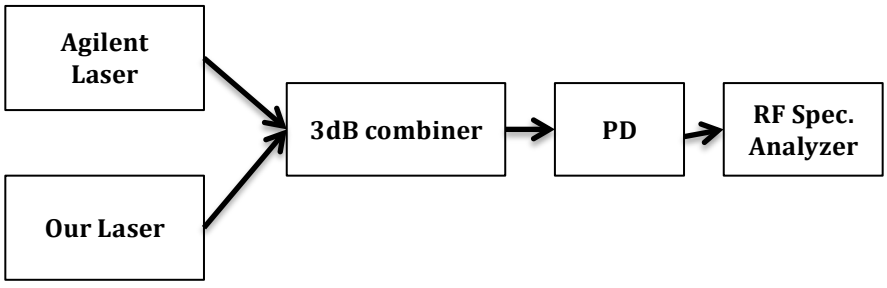

Figure 3.10 Heterodyne experiment diagram.

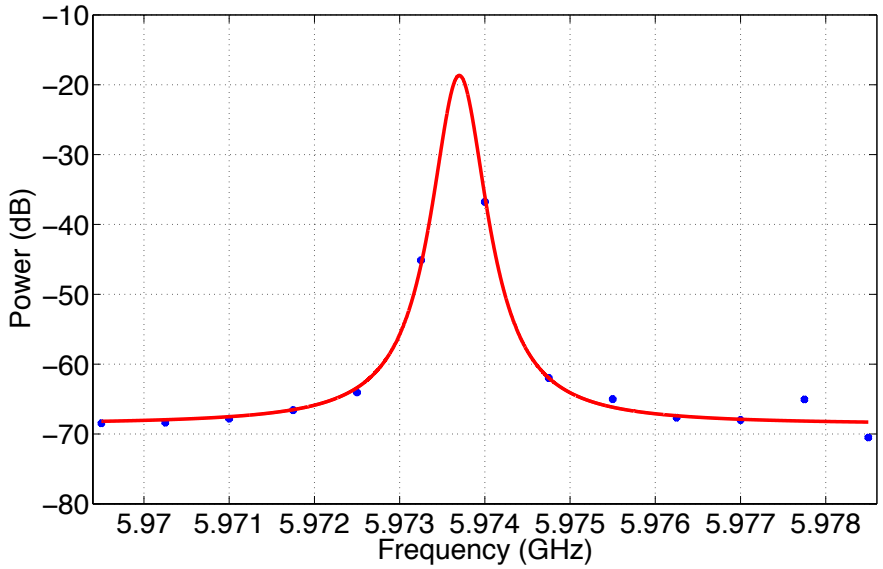

Figure 3.11 Heterodyne spectrum. Blue dots are experiment data, and red curve is Lorentz fit showing a combined linewidth of 220 kHz.

3.3.3 Relative Intensity Noise

Another metric of interest for the laser when used in data transmission system is the relative intensity noise (RIN). We characterized the RIN of our laser using the same PD and ESA as in the heterodyne measurement. We established an upper bound of the RIN at -135 dB/Hz across the RF spectrum range 20MHz-2.9GHz.

3.3.4 Tunability

Figure 3.12 shows the lasing spectra of our laser for different thermal tuning power applied to the ring resonator. Pump current was controlled at 80 mA to get an easier temperature control. Fig. 3.13 shows the center wavelength as a function of thermal tuning power. The lasing wavelength changes linearly as the tuning power increases. 6 nm of tuning wavelength range was obtained by about 6 mW of heating power. As the ring was thermally tuned, its resonance position, the wavelength with

most preferential feedback, red shifted. Since the cavity Fabry-Perot mode spacing was around 0.1 nm, about 60 longitudinal modes were progressively selected and deselected as the ring temperature changed. Some mode-hopping was seen during the tuning process, but the laser stayed stable at fixed locations. Mode hopping was most likely due to spontaneous change of filtering wavelength of the ring resonator and effective cavity length as tuning power was applied to the device. Heater resistance is 29 kΩ at low voltage. Current saturation is observed at voltages higher than 10 V due to the tiny size of the waveguide resistor. At 5.1 mW, the device local temperature is estimated to be about 120 ℃, comfortable below the level at which we'd expect damage to the device during the experiment. A number of results [7, 22], indicate that heating the ring up to over 250 ℃ without damaging silicon microrings, indicating that with improved resistors our device could achieve a tuning range of 15 nm or higher.

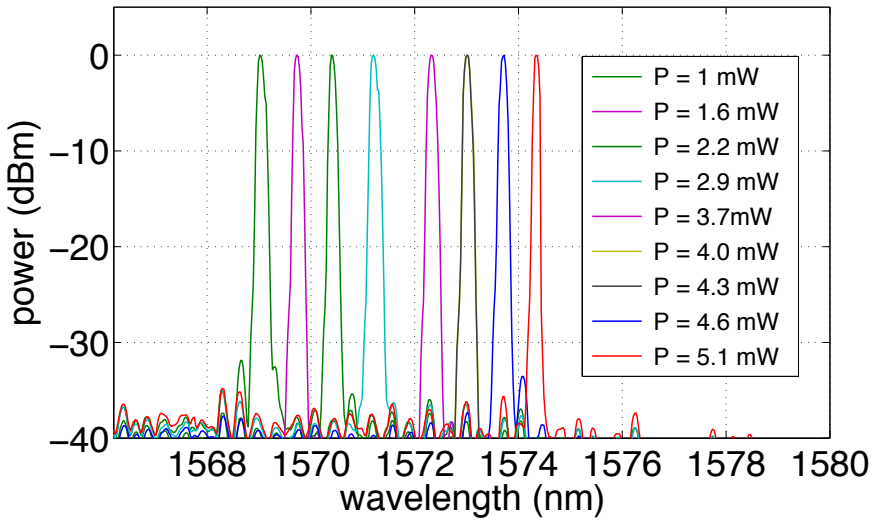

Figure 3.12 Measured lasing spectra of the tunable laser with various levels of thermal tuning power.

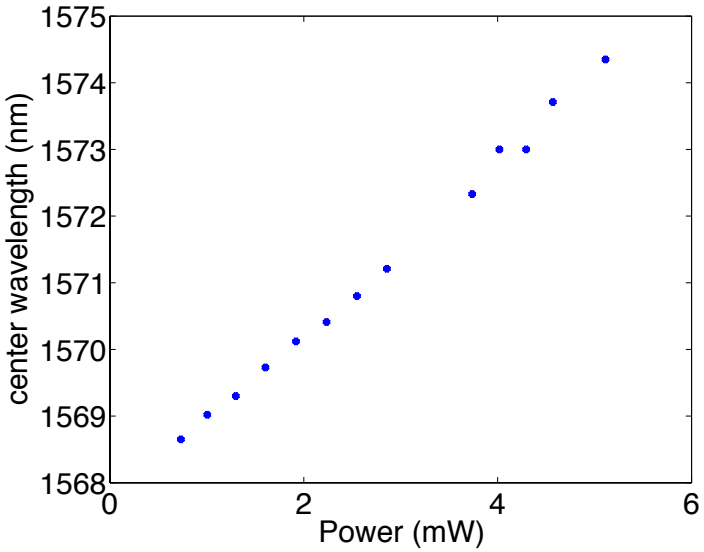

Figure 3.13 Center lasing wavelength as a function of heating power.

3.4 O-Band Laser with Sagnac Loop Mirror

3.4.1 Sagnac loop mirror

Ring resonance is very sensitive to the coupling strength, hence the mirror reflectivity is hard to control in the device described in the previous section. Then we come up with the Sagnac loop mirror based cavity configuration, as shown in Fig. 3.14. The micro-ring is fixed at critical coupling condition just for wavelength filtering, and the Sagnac loop mirror is used for broadband reflection. There is only one output, and the reflectivity can be accurate controlled by adjusting coupling length. The micro-filter and Sagnac loop mirror are independent and can be optimized separately. At the same time, it is a robust device, with low excess loss.

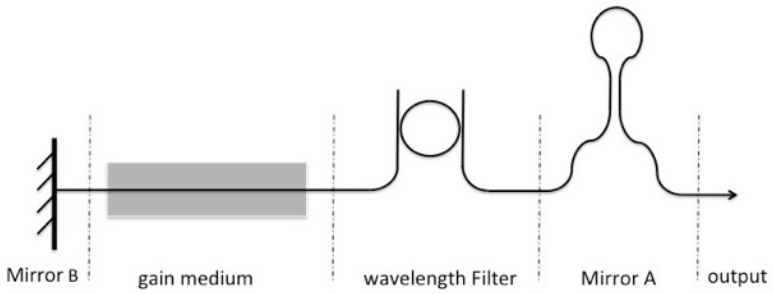

Figure 3.14 Diagram of Sagnac loop mirror based laser cavity configuration

The Sagnac loop mirror transmittance and reflectivity can be predicted analytically as it contains only a DC other than routing waveguide. Measured data match well with theory, as summarized in Fig. 3.15. Waveguide confinement decreases as the working wavelength is red shifted, hence evanescent coupling, and as a result the reflectivity of Sagnac loop mirror, is stronger in longer wavelength, as shown in the inset of Fig. 3.15(a).

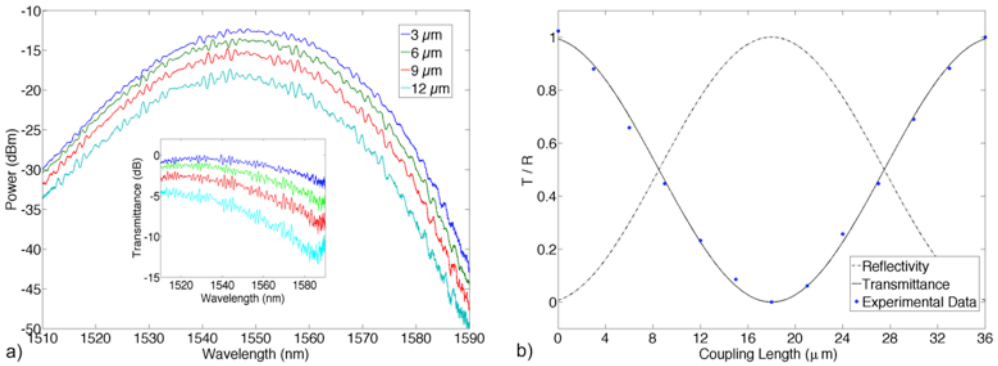

Figure 3.15 (a) Sagnac loop mirror transmission spectrum measured using a tunable laser and grating couplers; Normalized transmittance spectrum is shown in the inset; (b) Transmittance and reflectivity of Sagnac loop mirror as a function of DC coupling length at 1550 nm wavelength.

Almost all silicon photonics devices demonstrated to date operate in the C-Band (1530 nm to 1565 nm), which is within the fiber loss and erbium amplification window and ideal for long-haul communications. However, for short reach interconnects such as interconnect in data centers, the O-Band near 1310 nm is preferred to take advantage of the minimum dispersion window of standard optical fibers and is a widely used industry standard. It is possible to build silicon photonic components for O-band by leveraging knowledge of C-band devices, since passive components can be easily redesigned by scaling the geometry, the free carrier plasma effect used for electro-optical modulation is wavelength insensitive, and germanium in photodetectors has stronger absorption at shorter wavelengths. Building an integrated O-band laser source is important to complete the library of integrated devices.

Here I report the first hybrid integrated external cavity laser consisting of a quantum dot (QD) reflective semiconductor optical amplifier (RSOA) and a silicon on insulator (SOI) chip. Lasing at 1302 nm with over 50 dB side mode suppression ratio (SMSR) is observed. FWHM line width is less than 330 kHz determined by heterodyne measurement. We also demonstrate open-eye data transmission at 10 Gb/s and 40 Gb/s using this laser as the light source.

3.4.2 Gain Medium Integration

An appropriate gain medium must be used for building an O-Band light source, since the gain spectra of typical materials cannot cover both 1310 nm and 1550 nm. Conventional indium phosphide (InP) quantum well based gain medium could be used [23], but InAs/GaAs quantum dot gain medium gives unprecedented advantages, such as ultralow temperature dependence [24] and low-noise single cavity multi-wavelength lasing [25]. The wafer bonding approach in [23] mitigates alignment

efforts since waveguides are lithographically defined, but reduces CMOS compatibility at the same time. QD lasers monolithically grown on silicon were also reported [26], but compatibility with integration of the rest of silicon photonics device library remains elusive. We choose the external cavity laser approach by edge coupling a QD RSOA and a silicon chip, both of which can be optimized independently without compromising the performance. State-of-the-art optoelectronic packaging process can be leveraged to build the device cost effectively.

The diagram of our laser is shown in Fig. 3.14. The QD RSOA is based on indium arsenide quantum dots in gallium arsenide with aluminum gallium arsenide barriers and off-the-shelf commercially available [27]. Facet reflectivity is > 99% for the high reflective end and < 0.1% for the anti-reflective end, as specified by the manufacturer. The waveguide on the antireflective end is angled to reduce reflection into the laser cavity.

3.4.3 Silicon Chip Layout

On the SOI chip, the silicon device layer is 220 nm thick. 500 nm wide strip or rib waveguide is used for device layout and routing. The gap for evanescent coupling sections in the micro-ring wavelength filter and Sagnac loop mirror is 200 nm edge-to-edge. The Sagnac loop is a simple and robust on-chip mirror for silicon photonics. Its reflectivity can be tuned by adjusting the directional coupler, which in this case is made from two 15 μm long strip waveguides to provide about 50% reflection. The Lorentzian line shape of ring resonator provides strong side mode suppression and helps linewidth reduction [28]. The micro-ring may also be used for wavelength tuning and stabilization [18]. We used a micro-ring of radius 7.5 μm, with a coupling region containing a 1 μm-long rib waveguide directional coupler. Rib waveguide is

used for the ring as well to enable possible future electrode connections for wavelength tuning. The ring filter was measured to have an 8.8 nm free spectral range (FSR), and 0.8 nm FWHM bandwidth. The cavity length is dominated by the off-the-shelf RSOA length of 3 mm, which could be customized shorter in the future. The current cavity length corresponds to about 0.1 nm mode spacing, which is on the order of the FWHM of the micro-ring filter.

The laser out put is connected to a y-junction and grating coupler. Grating couplers were used because the insertion loss of a grating coupler could be more accurately and easily characterized than an edge coupler on our setup. A grating coupler loop, compared to a single grating coupler, helps fiber array alignment and measurement of grating coupler insertion loss. Insertion loss of the y-junction is well characterized, and could be easily normalized out.

To achieve low coupling loss, light in the silicon waveguide is first coupled to a silicon nitride waveguide using an inverse taper coupler. The inverse taper waveguide coupler has about 0.5 dB insertion loss. The silicon nitride waveguide is adiabatically tapered wider to match the RSOA mode size in the horizontal direction. In the vertical direction (normal to the wafer surface), 200 nm is too thin to provide effective mode confinement, and the modal field is extended into the oxide cladding to better match the RSOA mode. The nitride edge coupler mode size is designed to be 3.52 μm x 0.72 μm to match typical SOA mode sizes. The 200 nm-thick silicon nitride waveguide is less sensitive to fabrication errors compared to the 90 nm thick partially etched silicon waveguide we used in the previous section, and could be also used to build other devices, such as polarization splitter/rotators [29].

3.4.4 O-band laser characterization

The output pigtail fiber was connected to an optical spectrum analyzer. The observed lasing spectrum is plotted in Fig. 3.16. The lasing peak appears at 1302 nm, with over 50 dB side-mode suppression ratio (SMSR).

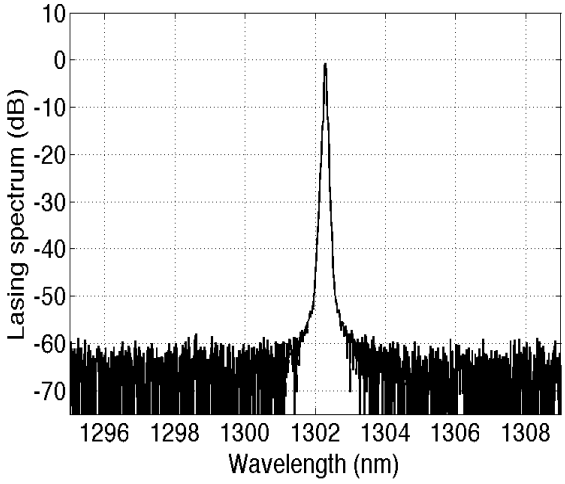

Figure 3.16 Laser optical spectrum. Lasing peak appear at 1302.2 nm

I then performed a heterodyne measurement of the linewidth of this device. The laser output was combined with the output of another laser, HP 8167A, using a 3 dB fiber coupler. Then the combined optical signal was fed into a photodetector. The photo current was fed into a RF spectrum analyzer. The heterodyne beating spectrum is plotted in Fig. 3.17, along with a Lorentz fit. According to the fit, the FWHM of the combined linewidth of DUT and HP 8167A is 330 kHz.

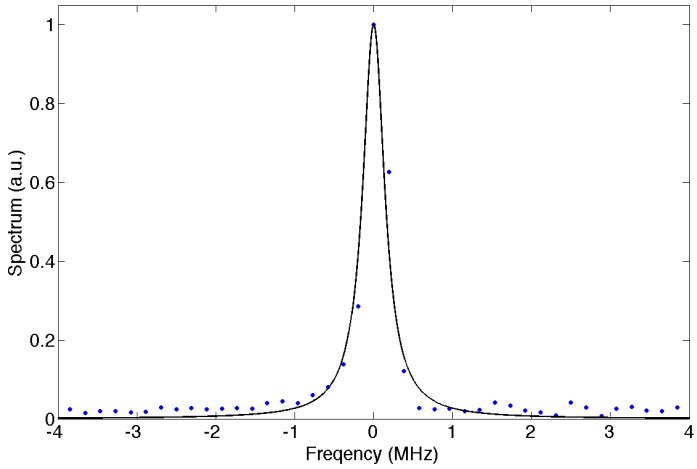

Figure 3.17 Heterodyne spectrum. Blue dots are experiment data, and black curve is a Lorentzian fit. The FWHM linewidth of the fit is 330 kHz

The light, voltage and current characteristics of this device are summarized in Fig. 3.18. A clear threshold is observed at around 90 mA. Some kinks due to mode hoping when the current is swept are also visible on the LI curve, a common occurrence for hybrid external silicon lasers. But the kink near 250 mA is irregular and most likely due to mechanical or thermally induced alignment perturbations. The coupling loss between silicon chip and RSOA is calculated to be 1.85 dB from the slope efficiency. The wall plug efficiency (WPE) at 200 mA is 5%, which is comparable to the devices in the literature [5-7] and could be further improved by adjusting the edge coupler to better match it mode, and putting anti-reflective coating on the silicon chip.

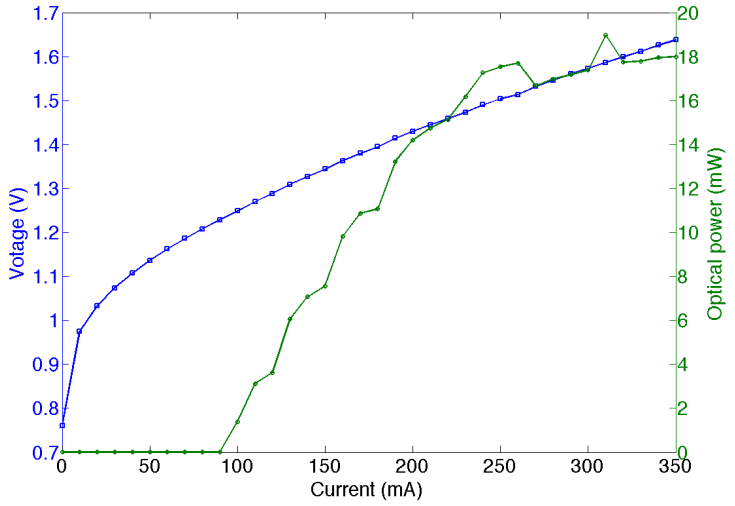

Figure 3.18 Laser bias voltage and output power as a function of pump current. Output power is measured using the fiber array, then normalized grating coupler and y-junction insertion loss

To further validate the viability of this device for data-com applications, we performed data transmission experiments at different data rates. The output of the DUT is first amplified and filtered, then modulated using a Lithium Niobate (LiNO3) Mach-Zehnder modulator. The non-return to zero (NRZ) modulated signal was received by a photodetector, and displayed on a digital communication analyzer (DCA). At 10 Gb/s, a clean and open eye diagram was observed, as shown in Fig. 3.19. Fig. 3.20 shows eye diagrams of our laser compared to a commercial DFB laser from Agere Systems (A1611A/B). Open eyes are observed showing suitable transmission, although with thicker lines and longer rise and fall times. Fig. 3.18 also indicates that the test equipment, instead of DUT, is limiting the speed.

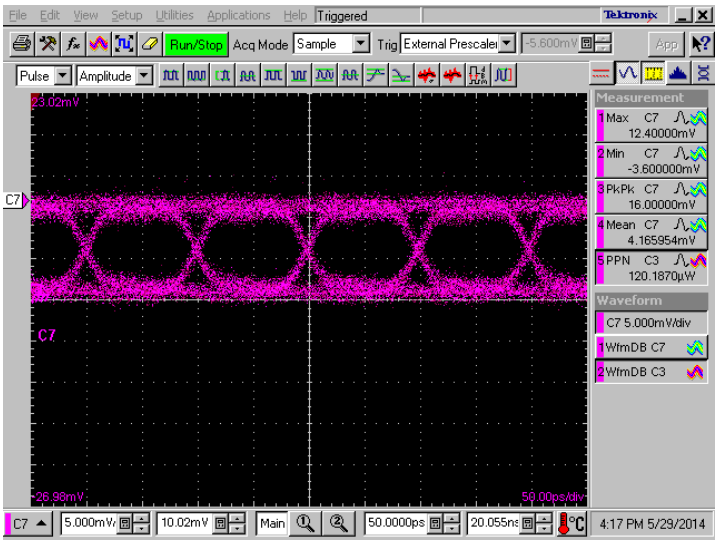

Figure 3.19 Eye Diagram at 10Gb/s

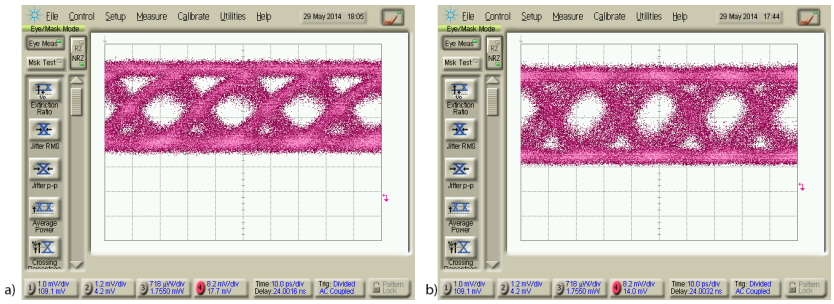

Figure 3.20 Eye diagrams at 40 Gb/s from: a) a commercial test laser and b) the device under test.

3.5 Ring Resonance Stabilization

In both devices, a microring resonator is used as intra cavity wavelength filters. Due to their resonance based operation, microrings offer intrinsic advantages such as small footprint, power efficiency, and wavelength division multiplexing (WDM) capability. However, the resonance also enhances the ring's sensitivity to

environmental temperature fluctuations. Overcoming this thermal sensitivity is necessary for commercial adaptation of microring devices.

Many researchers have worked on methods to compensate for microring thermal sensitivity. These projects have focused on (1) reducing the temperature sensitivity of the resonant structures using athermal materials, and (2) using integrated heaters combined with active feedback circuitry [18]. While successful, both of these approaches have drawbacks. The athermalizing approach uses novel materials to counteract the thermal optic coefficient of silicon, and requires additional manufacturing steps. While all existing active feedback approaches depends on the detection of optical power, which increases system cost due to the need for photodetectors, and requires optical power to function.

We present an active stabilization system based on measuring the absolute temperature of the microring using an integrated band-gap temperature sensor. Our approach extends earlier efforts to measure temperature on-chip [30] and does not require the presence of optical power to function. This type of control system has the potential to reduce cost and power consumption of microring based optical systems.

The microring device used in this study was fabricated at the A*STAR Institute of Microelectronics (IME) via an OpSIS multi-project-wafer run. The process uses an 8” Silicon-on-Insulator (SOI) wafer from SOITEC with 220 nm top silicon layer and 2 μm bottom oxide. The device is a modification of existing microring modulator designs demonstrated in the OpSIS platform and did not require process modifications. It contains a high-speed modulation junction, a resistive integrated heater, and two matched narrow p-n junctions for temperature sensing (Fig. 3.21(a)).

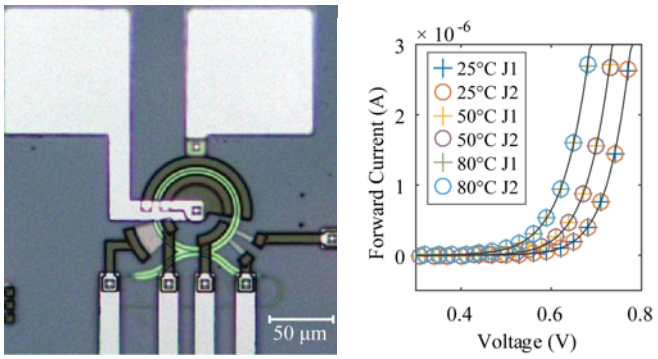

Figure 3.21 (a) Fabricated microring modulator viewed through a microscope. The matched pn-junctions used for temperature sensing are on the lower right quadrant of the device, while the integrated heater is in the lower left, and the high-speed modulation junction covers the top semicircle. (b) IV curves of the two junctions under different temperatures. The junctions match perfectly.

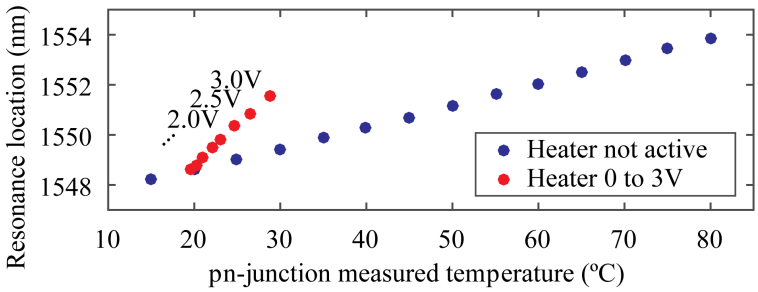

Figure 3.22 Microring resonance location vs. temperature measured by the pn-junction. The pn-junction accurately measures the microring temperature when the integrated heater is not active (blue). However, when the integrated heater is used to heat up the ring while the global temperature is held constant (as an example, at 20 ºC for the red curve), the relationship between measured temperature and resonance location is skewed.

Temperature measurement can be performed by forward biasing the matched pn-junctions at different currents then measuring the difference in forward voltages [31]. Due to the matching of the junctions (Fig. 3.21(b)) the voltage difference is

linearly correlated to the absolute temperature of the junction. We measured the temperature of the microring by biasing one junction at 1 μA and the other at 10 μA. The temperature thus measured shows excellent agreement with optically measured ring resonance location (Fig. 3.22). However, an interesting problem occurred when the integrated heater was used to heat the microring. The red curve in Fig. 3.22 shows the pn-junctions measuring a lower temperature than the true temperature of the microring when heater power is applied. We suspect that a thermal gradient builds up around the integrated heater, causing the microring to experience an aggregate temperature change greater than that measured at the junction.

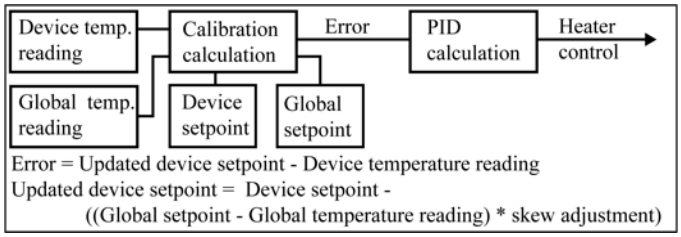

Figure 3.23 Block diagram of the feedback controller used in the experiment. Device temperature is the reading from the sensor in the ring, and global temperature is the reading from the second sensor. The two setpoints are constants, and the skew adjustment factor is found using slopes interpreted from Fig. 3.22. The measured change in global temperature is used to update the target temperature for the sensor in the ring.

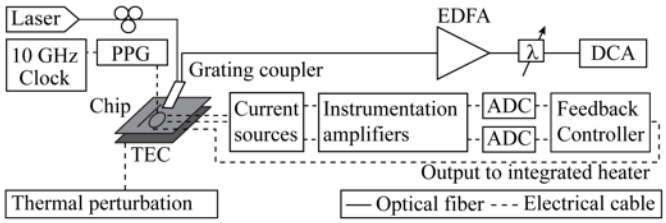

Figure 3.24 Experimental setup to demonstrate temperature stabilization.

Due to the skewed temperature reading from the pn-junctions, a traditional proportional-integral-derivative (PID) feedback controller will not be able to stabilize the microring using the integrated heater. Any change in the environmental temperature would cause the PID controller to overreact and change the resonance too much. What is needed is a way to calibrate for the effect of integrated heater on the sensor.

We accomplished this calibration by using a second pair of matched pn-junctions on the chip located 300 μm away from the microring. This second senor is close enough to the ring to be similarly affected by global temperature changes, but remains far enough away to not be affected by the integrated heater. Combining this secondary information with the skewed but still useful reading from the original pair of pn-junctions, a PID controller can close the loop to stabilize the microring. Fig. 3.23 shows a block diagram of the feedback controller and the calibration algorithm.

Fig. 3.24. shows the experimental setup of the experiment. The chip containing the microring modulator was attached to a thermal-electric-cooler (TEC) using thermal adhesive. The global temperature of the TEC can be modified at ~0.3 K/s with a driving current of 1 A. A laser was coupled into the device using a grating coupler, and low speed probes were used to contact the pn-junctions and integrated heater. 10 GB/s data modulation was achieved using high speed probes with a reverse bias of -2.8 V and a 5.5 Vpp driving signal.

The pairs of pn-junctions were forward biased using LM234Z programmable current sources, and the output voltages were amplified using INA116PA instrumentation amplifiers. The feedback controller and calibration calculation were performed using a PIC24H microcontroller, which has built-in 16-bit analog-to-digital

converters (ADC) and 10-bit digital-to-analog converters (DAC). The feedback system ran at a sampling rate of 80 Hz and consumed a maximum power of 7 mW, without counting the dissipated heater power.

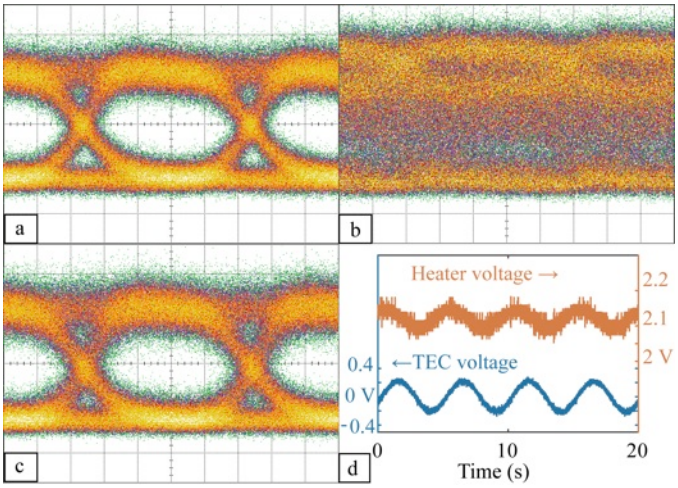

Figure 3.25 (a) 10 Gb/s eye diagrams without thermal perturbation, (b) with thermal perturbation but without stabilization, and (c) with thermal perturbation and thermal stabilization enabled. (d) Heater voltage during feedback control. There is a ~1 second delay for the TEC temperature change to propagate to the microring.

Fig. 3.25(d) shows the feedback system in action against a thermal shift of 1.0 K. The bottom curve is the control voltage of the TEC, where a positive voltage is an increase in temperature and negative a decrease. The top curve shows the heater voltage generated by the feedback controller. Using the calibration routine the feedback system was able to correctly compensate for the temperature variation. Eye diagrams with and without the active thermal feedback is shown in Fig. 3.25(a)-(c), demonstrating successful thermal stabilization.

3.6 Summary

In this Chapter, a single adiabatic microring based external cavity laser using reflective SOA and a silicon photonics chip is demonstrated. The laser worked at 1570 nm, and was measured to have 9.8 mW on-chip output power, less than 220 kHz linewidth, over 45 dB side mode suppression ratio. To make it easier to adjust the reflectivity of the on-chip partial reflective mirror, a Sagnac loop based laser cavity is proposed and characterized. A laser working at 1302 nm is also presented for O-Band applications. Sagnac loop mirror and microring based laser cavity configuration is utilized in the O-Band device. Open eye diagrams at 10 and 40 Gb/s are demonstrated. In both devices, a microring resonator is used as intra cavity wavelength filter, whose resonant wavelength drifts as temperature varies. I show resonant wavelength stabilization solution based on band gap temperature sensor and active feedback control.

REFERENCES

1. J. Zilkie, P. Seddighian, B. J. Bijlani, W. Qian, D. C. Lee, S. Fathololoumi, J. Fong, R. Shafiiha, D. Feng, B. J. Luff, X. Zheng, J. E. Cunningham, A. V. Krishnamoorthy, and M. Asghari, "Power-efficient III-V/Silicon external cavity DBR lasers," Opt. Express 20(21), 23456-23462 (2012).
2. S. Tanaka, S. H. Jeong, S. S., T. Kurahashi, Y. Tanaka, and K. Morito, "High-output-power, single-wavelength silicon hybrid laser using precise flip-chip bonding technology," Opt. Express 20(27), 28057-28069 (2012).
3. K. Nemoto, T. Kita, and H. Yamada, "Narrow-Spectral-Linewidth Wavelength-Tunable Laser Diode with Si Wire Waveguide Ring Resonators," Appl. Phys. Express 5, 082701 (2012).
4. R. M. Oldenbeuving, E. J. Klein, H. L. Offerhaus, C. J. Lee, H. Song, and K-J. Boller, "25 kHz narrow spectral bandwidth of a wavelength tunable diode laser with a short waveguide-based external cavity," Laser Phys. Lett., 10, 015804 (2012).
5. T. Creazzo, E. Marchena, S. B. Krasulick, P. Yu, D. Van Orden, J. Y. Spann, C. C. Blivin, L. He, H. Cai, J. M. Dallesasse, R. J. Stone, and A. Mizrahi, "Integrated tunable CMOS laser," Opt. Express 21(23), 28048-28053 (2013).
6. X. Zheng, S. Lin, Y. Luo, J. Yao, G. Li, S. S. Djordjevic, J. Lee, H. D. Thacker, I. Shubin, K. Raj, J. E. Cunningham and A. V. Krishnamoorthy, "Efficient WDM Laser Sources towards Terabyte/s Silicon Photonic Interconnects," J. Lightwave Technol., 31(24), 4142-4154 (2013).
7. S. Lin, S. S. Djordjevic, J. E. Cunningham, I. Shubin, Y. Luo, J. Yao, G. Li, H. D. Thacker, J. Lee, K. Raj, X. Zheng, and A. V. Krishnamoorthy, "Vertical-coupled high-efficiency tunable III-V-CMOS SOI hybrid external-cavity laser," Opt. Express 21(26), 32425-32431 (2013).

8. Biberman, E. Timurdogan, W. A. Zortman, D. C. Trotter,and M. R. Watts, "Adiabatic microring modulators," Opt. Express 20(28), 29223-29236 (2012).
9. M. Gould, A. Pomerene, C. Hill, S. Ocheltree, Y. Zhang, T. Baehr-Jones, and M. Hochberg, "Ultra-thin silicon-on-insulator strip waveguides and mode couplers," Appl. Phys. Lett. 101, 221106 (2012).
10. X. Wang, W. Shi, H. Yun, S. Grist, N. A. F. Jaeger, L. Chrostowski, "Narrow-band waveguide Bragg gratings on SOI wafers with CMOS-compatible fabrication process", Opt. Express 20(14), 15547-15558 (2012).
11. G. T. Paloczi, J. Scheuer, and A. Yariv, "Compact Microring-Based Wavelength-Selective Inline Optical Reflector," IEEE Photon. Technol. Lett. 17, 390-392 (2005).
12. W. Shi, H. Yun, W. Zhang, C. Lin, T. K. Chang, Y. Wang, N. A. F. Jaeger, L. Chrostowski, "Ultra-compact, high-Q silicon microdisk reflectors," Opt.Express 20(20), 21840-21846 (2012).
13. V. Krishnamoorthy,X. Zheng, G. Li, J. Yao, T. Pinguet, A. Mekis, H. Thacker, I. Shubin, Y. Luo, K. Raj, and J. E. Cunningham, "Exploiting CMOS manufacturing to reduce tuning requirements for resonant optical devices," IEEE Photon. J. 3(3), 567-579 (2011).
14. M. R. Watts, "Adiabatic Microring-Resonators," Opt. Letters 35(19), 3231-3233 (2010).
15. J. C. Mikkelsen, W. D. Sacher, and J. K.-S. Poon, "Adiabatically widened silicon microrings for improved variation tolerance," Opt. Express 22(8), 9659-9666 (2014).
16. S. K. Selvaraja, P. Jaenen, W. Bogaerts, D. Van Thourhout, P. Dumon, and R. Baets, "Fabrication of photonic wire and crystal circuits in silicon-on-insulator using 193-nm optical lithography," J. Lightw. Technol. 27(18), 4076-4083 (2009).
17. S.-H. Jeong, D. Shimura, T. Simoyama, M. Seki, N. Yokoyama, M. Ohtsuka, K. Koshino, T. Horikawa, Y. Tanaka, and K. Morito, "Low-loss, flat-topped

and spectrally uniform silicon-nanowire-based 5th-order CROW fabricated by ArF-immersion lithography process on a 300-mm SOI wafer," Opt. Express 21(25), 30163-30174 (2013).

18. K. Padmaraju, J. Chan, L. Chen, M. Lipson, and K. Bergman, "Thermal stabilization of a microring modulator using feedback control," Opt. Express 20(27), 27999-28008 (2012).
19. P. Dong, W. Qian, H. Liang, R. Shafiiha, D. Feng, G. Li, J. E. Cunningham, A. V. Krishnamoorthy, and M. Asghari, "Thermally tunable silicon racetrack resonators with ultralow tuning power," Opt. Express 18(19), 20298-20304 (2010).
20. K. Kallimani and M.J.OrMahony, "Calculation of optical power emitted from a fiber grating laser," IEE Proc. Optoelectron 145, 319-324 (1998).
21. H. Henry, “Theory of the linewidth of semiconductor lasers,” IEEE J. Quantum Electron. 18(2), 259-264 (1982)
22. J. Sun, E. Timurdogan, A. Yaacobi, E. S. Hosseini, and M. R. Watts, "Large-scale nanophotonic phased array," Nature 493, 195-199 (2013).
23. H.-H. Chang, A. W. Fang, M. N. Sysak, H. Park, R. Jones, O. Cohen, O. Raday, M. J. Paniccia, and J. E. Bowers, “1310nm silicon evanescent laser,” Opt. Express 15(18), 11466-11471 (2007).
24. Y. Tanaka, M. Ishida, K. Takada, T. Yamamoto, H. Song, Y. Nakata, M. Yamaguchi, K. Nishi, M. Sugawara, and Y. Arakawa, “25 Gbps direct modulation in 1.3-μm InAs/GaAs high-density quantum dot lasers,” Conf. on Lasers and Electro-Optics (CLEO), Paper CTuZ1, 2010.
25. G. L. Wojcik, D. Yin, A. R. Kovsh, A. E. Gubenko, I. L. Krestnikov, S. S. Mikhrin, D. A. Livshits, D. A. Fattal, M. Fiorentino, R. G. Beausoleil, "A single comb laser source for short reach WDM interconnects,” Proc. SPIE 7230, Novel In-Plane Semiconductor Lasers VIII, 72300M (2009).

26. T. Wang, H. Liu, A. Lee, F. Pozzi, and A. Seeds, “1.3-μm InAs/GaAs quantum-dot lasers monolithically grown on Si substrates,” Opt. Express 19(12), 11381-11386 (2011).
27. http://www.innolume.com/products/Gain-chips.htm.
28. Liu, A. Shakouri, and J. E. Bowers, “Passive microring-resonator-coupled lasers,” Appl. Phys. Lett. 79(22), 3561-3563 (2001).
29. L. Chen, C. R. Doerr, and Y.-K. Chen, “Compact polarization rotator on silicon for polarization-diversified circuits,” Opt. Letters 36(4), 469-471 (2011)
30. DeRose, M. Watts, D. Trotter, D. Luck, G. Nielson, and R. Young, “Silicon Microring Modulator with Integrated Heater and Temperature Sensor for Thermal Control,” CLEO, 2010, CThJ3
31. J. Millman and C.C. Hahas, Electronic devices and circuits, New York, McGraw Hill Book Co., 1967, Ch. 6,pp. 131-132.

Chapter 4

MULTI-WAVELENGTH LASER

During testing the external cavity lasers in Chapter 3, multiple lasing peaks were sometimes observed, although they were not stable due to mode competition. A comb laser source substitutes for an array of lasers and WDM multiplexers and can potentially reduce the packaging cost of silicon photonics transceivers. In this Chapter, I report a multi-wavelength laser using a quantum dot RSOA and silicon photonics chip. I am in charge of the device design and testing. I would like to thank Dr. Yi Zhang in our group for helpful discussions, especially on selecting the quantum dot gain chip and located the vendor. Four lasing peaks with less than 3 dB power non-uniformity were measured, and error free 4 × 10 Gb/s data transmission using the multi-wavelength laser as the light source was demonstrated.

4.1 Ring Based WDM System

Microring resonator is a unique device enabled by submicron silicon waveguide and the high index contrast between silicon and silicon oxide. Microring modulators can be more energy efficient, and orders of magnitude smaller than travelling wave Mache-Zehnder modulators [1,2]. Microrings are also widely used as wavelength filters and multiplexers, which are compact and thermally tunable [3]. High-order ring filters with flattened top and steep out-of-band rejection have also been reported [4]. Ring resonance stabilization that mitigates thermal and fabrication sensitivity has been demonstrated as well [5]. Another major advantage of the

microring is its intrinsic wavelength division multiplexing (WDM) capability. A microring based WDM data transmission system is illustrated in Fig. 4.1. On the transmitter side, light at different frequencies from a comb source is modulated by multiple ring modulators on a common bus waveguide. On the receiver side, signal in different channels is first dropped using a microring filter, and then fed into a photodetector. High performance microring modulators [1,2], wavelength filters [3,4] and germanium photodetectors [6,7] have been extensively studied.

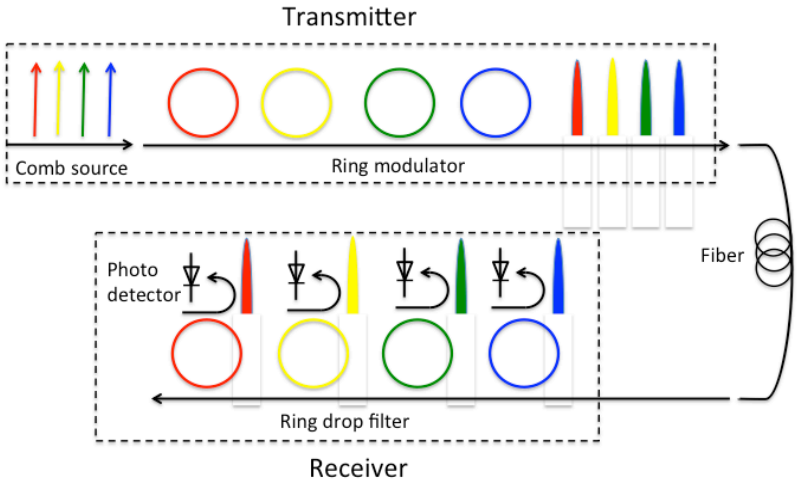

Figure 4.1 Schematic of a microring based WDM data transmission system.

Having an integrated comb source is critical to the microring based WDM transceiver, but such source still remains elusive in the literature. A comb source could be made of an array of lasers followed by a wavelength multiplexer [8,9], but laser arrays are usually expensive due to the limited yield and relatively low manufacturing volumes of III/V single-mode compound devices. The other option is to use a single laser that simultaneously generates multiple lasing peaks. One way to build such a

multi-wavelength laser is to utilize fiber nonlinearity. Successful generation of 1520 wavelengths and 31.8 Tb/s transmission was demonstrated in [10]. But nonlinear fiber based comb sources are bulky and hard to integrate. Monolithic nonlinear comb sources demonstrated [11-12] are promising for sensing and metrology, but their efficiency needs to be significantly improved for data transmission. Conventional semiconductor Fabry-Perot (FP) lasers support multiple longitudinal modes, but the amplitude of each mode can fluctuate significantly even if the total power is stable, due to competition for optical gain among different longitudinal modes, which is also called mode partitioning [13]. Thus an individual longitudinal mode in FP lasers cannot be modulated for data transmission [14]. More recently, it was reported that quantum dot (QD) FP lasers have much lower mode partition noise due to strong spectral hole burning [15-17]. While QD FP lasers seem like they could be a plausible multi-wavelength source, they are not directly integrable into a silicon photonics transceiver. The flexibility of having part of the cavity in the silicon opens the possibility of convenient channel spacing selection, linewidth reduction, efficient thermal wavelength tuning, direct integration with transceivers, and many other applications.

In this chapter, I report the first external cavity multi-wavelength laser fabricated by integrating a QD reflective semiconductor optical amplifier (RSOA) and a silicon photonics chip. The QD RSOA is the gain medium with low mode partition noise, while a half-cavity on the silicon chip provides lithographically defined wavelength selective reflection. We show four major lasing peaks near 1300 nm. Error-free data transmission on each wavelength is also demonstrated.

4.2 Device Design

The diagram of the laser is shown in Fig. 4.2. The QD RSOA is based on Indium Arsenide quantum dots in Gallium Arsenide with Aluminum Gallium Arsenide barriers, and is commercially available [18]. It has a specified facet reflectivity is > 99% for the high reflective end and < 0.1% for the anti-reflective end. The waveguide on the anti-reflective end is also curved to reduce reflection into the cavity. A photo of the QD RSOA chip, together with the rest of the device setup, is shown in Fig. 4.3. The half-cavity on the silicon chip consists of a Sagnac loop mirror and a microring wavelength filter. The Sagnac loop is made by connecting two waveguide on one side of a directional coupler, which is a simple and robust way to build on-chip mirrors in silicon [19]. Its reflectivity can be accurately controlled by setting the proper coupling length in the directional coupler. In this device, the two strip waveguides in the directional coupler are 500 nm wide, 220 nm thick, and separated by 200 nm edge to edge. Coupling length is set to 15 μm to achieve 50% reflection. However, a Sagnac loop mirror only provides broadband reflection, so a microring wavelength filter is inserted in the cavity for wavelength selection. The ring radius is 35 μm, with 2 μm straight waveguide in coupling region, corresponding to a free spectral range (FSR) of 2 nm. The measured transmission spectrum of this microring filter is shown in black dashed line in Fig. 4.4. The Y-junction in between the two grating couplers is a well-characterized device, and it enables us to measure the grating coupler efficiency using a commercial test laser.

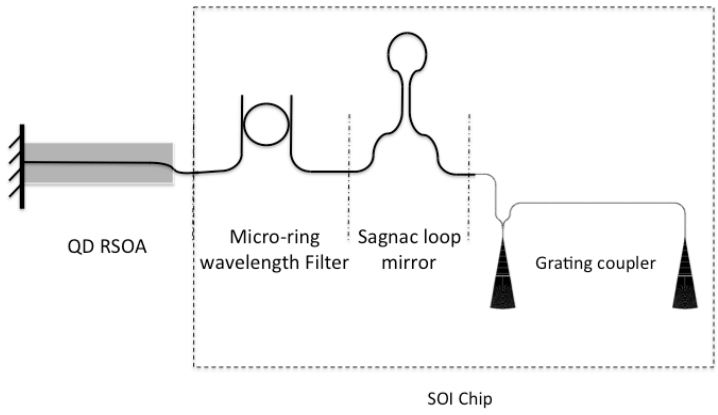

Figure 4.2 Diagram of the QD RSOA / silicon hybrid multi-wavelength laser.

To reduce the coupling loss at the RSOA/silicon interface, light in the submicron silicon waveguide is first coupled into a silicon nitride waveguide using an inverse taper. The silicon nitride waveguide is adiabatically tapered wider in the horizontal direction to match the RSOA waveguide width. In the vertical dimension, the nitride waveguide is only 200 nm thick, which leads to a much lower confinement factor and allows the modal field to extend into the oxide cladding to better match the RSOA mode. The designed nitride waveguide mode field diameter is 3.5 μm × 0.7 μm, close to a typical SOA mode size.

4.3 Device Characterization

4.3.1 Chip alignment

The silicon chip was polished after wafer dicing to create a flat and smooth facet for butt coupling. No anti-reflective coating was applied on the silicon chip. Then both the RSOA and the silicon chip were mounted on six-axis stages for alignment. The RSOA chip was kept at 25 °C using a thermo-electric cooler (TEC),

while the silicon chip remained at the ambient temperature of the metal stage. 210 mA of pump current was provided to the RSOA from a DC source during alignment. A lensed fiber coupled to the 0.1% anti-reflective facet was used to monitor the cavity ASE or lasing power as a feedback for active alignment. After the QD RSOA and silicon chip were properly aligned, a fiber array was brought in to capture the output from the grating coupler. An image of the testing setup is shown in Fig. 4.3, as well as a zoomed-in view of the silicon chip/RSOA interface.

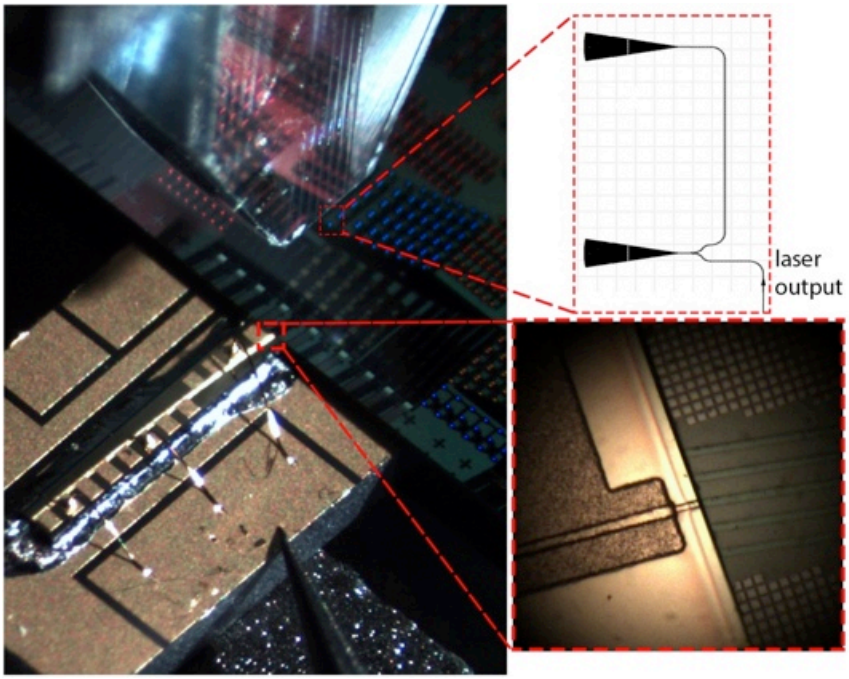

Figure 4.3 Image of the alignment setup (left), and a zoomed-in view of the RSOA / silicon chip interface (lower right). A schematic of the grating coupler on chip is shown top right, containing a Y-junction and an additional output coupler to assist fiber array coupling. The fiber array can be seen in the top left of the figure.

4.3.2 Laser spectrum and LIV

The output of the fiber array was connected to an optical spectrum analyzer. The displayed spectrum is plotted in Fig. 4.4, as well as the intra-cavity microring filter transmission spectrum. Multiple lasing peaks were demonstrated, and the laser mode spacing matches the FSR of the microring filter, which is 2 nm as mentioned earlier. Four major lasing peaks were observed between 1300 nm and 1308 nm, with less than 3 dB power non-uniformity.

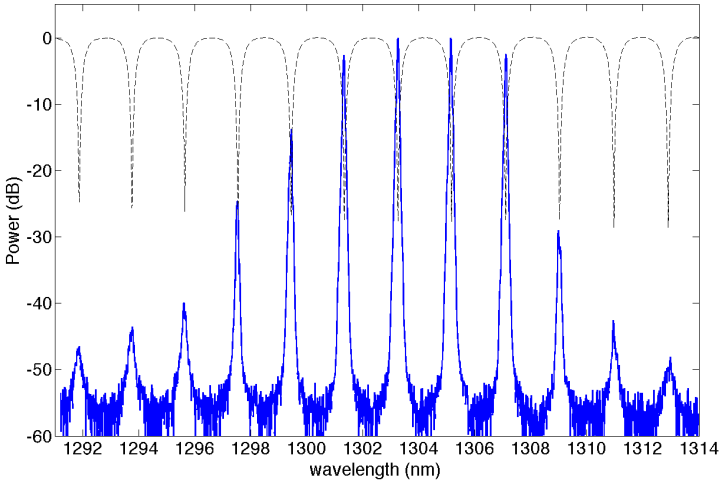

Figure 4.4 Laser spectrum (solid blue line) and microring filter transmission spectrum (dashed black line).

The laser LIV characteristics are shown in Fig. 4.5. The blue line shows a typical rectifying IV curve of a p-n diode, and the red line indicates a threshold current of 60 mA. The on-chip output power at 200 mA, about three times the threshold, is 20 mW, corresponding to a wall-plug efficiency (WPE) of 5.9%.

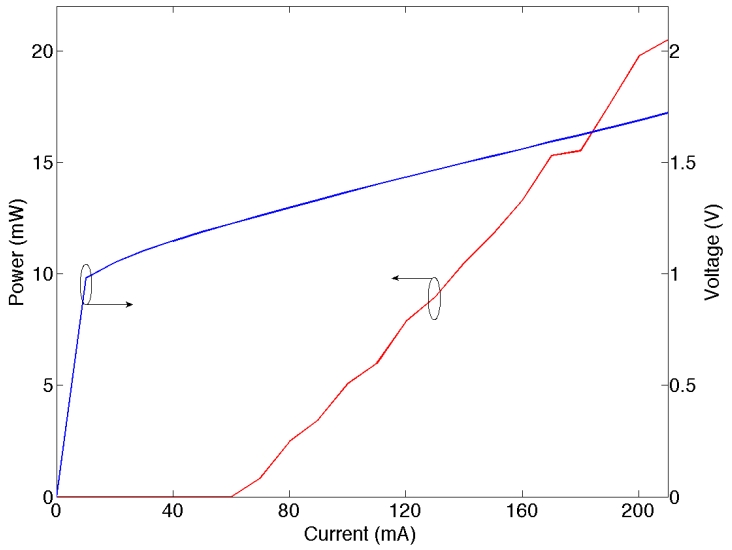

Figure 4.5 Laser output power (red) and forward bias voltage (blue) as a function of drive current.

4.3.3 Data transmission experiment

To validate the viability of the multi-wavelength laser for WDM data communication applications, each laser peak was filtered out using a tunable filter and modulated using a Lithium Niobate Mache-Zehnder modulator. The data stream used for modulation is a 10 Gb/s non-return to zero (NRZ) 27-1 pseudo random bit sequence (PRBS). The modulated optical signal was split into two branches. One branch was amplified using a Praseodymium-doped-fiber-amplifier (PDFA) and displayed on a digital communication analyzer (DCA). The other branch was first connected to a variable optical attenuator, then an avalanche photodetector (APD) and a bit error rate tester (BERT). The eye diagrams from the 4 lasing peaks are shown Fig. 4.6(a)-(d), along with the filtered spectrum of one of the peaks Fig. 4.6(f). Eye diagram of a control experiment conducted using a commercial 1310 nm laser is

shown in Fig. 4.6(e). Open eye diagrams are observed on all four channels, qualitatively confirming successful data transmission. Testing configuration illustrated in Fig. 4.7(a). Recorded bit error rate (BER) as a function of received power is plotted in Fig. 4.7(b). At 10-9 bit error rate, all channels have less than 2.6 dB power penalty compared to the commercial laser. We note that the eye diagrams and receiver sensitivity from different channels are slightly non-uniform most likely because the relative position of the RSOA and silicon chip was drifting over the period of the BER measurement. This drift could be eliminated by bonding the RSOA and silicon chips together using epoxy or by upgrading our alignment stages.

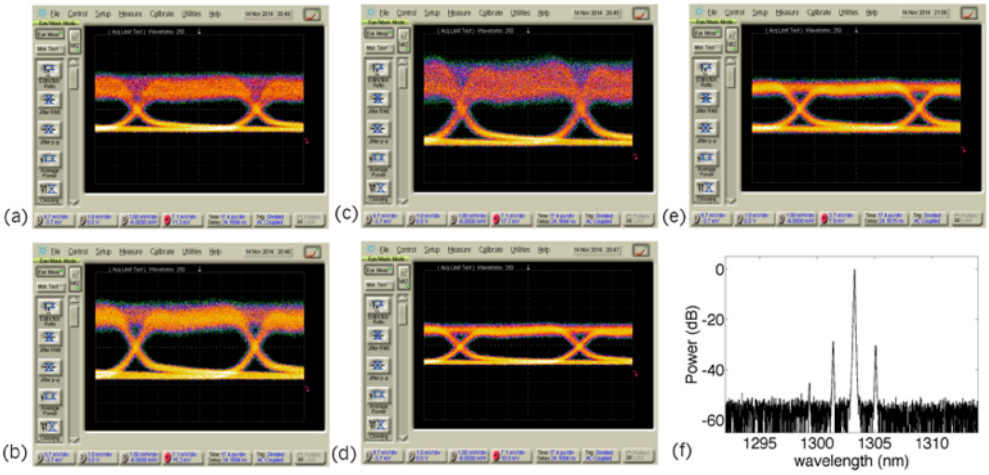

Figure 4.6 (a)-(d) corresponds to channel 1-4, (e) is control experiment using commercial DFB, and (f) is one filtered spectrum.

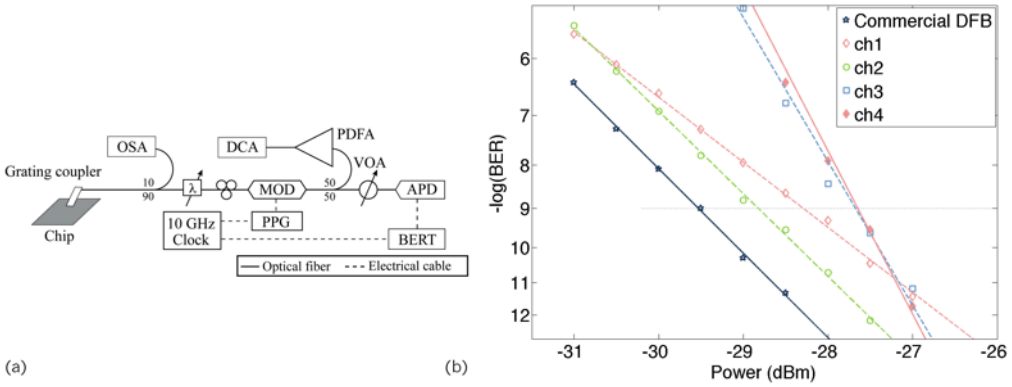

Figure 4.7 Testing configuration diagram and bit error rate as a function of received power.

4.4 Summary

A single cavity multi-wavelength laser is demonstrated on silicon. The multi-wavelength external cavity laser consists of a quantum dot (QD) RSOA and a silicon photonics chip. QD RSOA offers much lower mode partition noise compared to conventional bulk or quantum well gain medium due to strong spectral whole burning. The silicon photonics chip provides partial reflective mirror with multiple pass bands. Four lasing peaks with less than 3 dB power non-uniformity were measured, and error free 4 × 10 Gb/s data transmission using the multi-wavelength laser as the light source was demonstrated. This multi-wavelength paves the way for a complete microring based WDM solution in silicon photonics.

REFERENCES

1. Q. Xu, B. Schmidt, S. Pradhan, and M. Lipson, "Micrometre-scale silicon electro-optic modulator," Nature 435, 325-327 (2005).
2. G. Li, A. V. Krishnamoorthy, I. Shubin, J. Yao, Y. Luo, H. Thacker, X. Zheng, K. Raj, and J. E. Cunningham, "Ring resonator modulators in silicon for interchip photonic links," IEEE J. Sel. Topics Quantum Electron. 19(6), 3401819 (2013).
3. P. Dong, W. Qian, H. Liang, R. Shafiiha, D. Feng, G. Li, J. E. Cunningham, A. V. Krishnamoorthy, and M. Asghari, "Thermally tunable silicon racetrack resonators with ultralow tuning power," Opt. Express 18(19), 20298-20304 (2010).
4. S.-H. Jeong, D. Shimura, T. Simoyama, M. Seki, N. Yokoyama, M. Ohtsuka, K. Koshino, T. Horikawa, Y. Tanaka, and K. Morito, "Low-loss, flat-topped and spectrally uniform silicon-nanowire-based 5th-order CROW fabricated by ArF-immersion lithography process on a 300-mm SOI wafer," Opt. Express 21(25), 30163-30174 (2013).
5. K. Padmaraju, J. Chan, L. Chen, M. Lipson, and K. Bergman, "Thermal stabilization of a microring modulator using feedback control," Opt. Express 20(27), 27999-28008 (2012).
6. L. Vivien, A. Polzer, D. Marris-Morini, J. Osmond, J. M. Hartmann, P. Crozat, E.Cassan, C. Kopp, H. Zimmermann, and J. M. Fédéli, "Zero-bias 40Gbit/s germanium waveguide photodetector on silicon," Opt. Express 20(2), 1096-1101 (2012).
7. Y. Zhang, S. Yang, Y. Yang, M. Gould, N. Ophir, A. E.-J. Lim, G.-Q. Lo, P. Magill, K. Bergman, T. Baehr-Jones, and M. Hochberg, "A high-responsivity

photodetector absent metal-germanium direct contact," Opt. Express 22(9), 11367-11375 (2014).

8. G. Kurczveil, M. J. R. Heck, J. D. Peters, J. M. Garcia, D. Spencer, and J. E. Bowers, "An integrated hybrid silicon multiwavelength AWG laser," IEEE J. Sel. Topics Quantum Electron. 17(6), 1521-1527 (2011).
9. S. Keyvaninia, S. Verstuyft, S. Pathak, F. Lelarge, G.-H. Duan, D. Bordel, J.-M. Fedeli, T. De Vries, B. Smalbrugge, E. J. Geluk, J. Bolk, M. Smit, G. Roelkens, and D. Van Thourhout, "III-V-on-silicon multi-frequency lasers," Opt. Express 21(11), 13675-13683 (2014).
10. V. Ataie, E. Temprana, L. Liu, Y. Myslivets, P. Kuo, Ni. Alic, and S. Radic, "Flex-grid compatible ultra wide frequency comb source for 31.8 Tb/s coherent transmission of 1520 UDWDM channels," in Optical Fiber Communication Conference, paper Th5B (2014).
11. P. Del'Haye, A. Schliesser, O. Arcizet, T. Wilken, R. Holzwarth, and T. J. Kippenberg, "Optical frequency comb generation from a monolithic microresonator," Nature 450, 1214–1217 (2007).
12. M. A. Foster, J. S. Levy, O. Kuzucu, K. Saha, M. Lipson, and A. L. Gaeta, "Silicon-based monolithic optical frequency comb source," Opt. Express 19(15), 14233-14239 (2011).
13. C. H. Henry, P. S. Henry, and M. E. Lax, "Partition fluctuations in nearly single-longitudinal-mode lasers," J. Lightw. Technol. LT-2(3), 209-215 (1984).
14. Y. Okano,K. Nakagawa, and T. Ito, "Laser mode partition noise evaluation for optical fiber transmission," IEEE Trans. Commun. 28(2), 238-243 (1980).
15. A. Kovsh, I. Krestnikov, D. Livshits, S. Mikhrin, and J. Weimert, "Quantum dot laser with 75 nm broad spectrum of emission," Opt. Lett. 32(7), 793-795 (2007).
16. A. Gubenko, I. Krestnikov, D. Livshtis, S. Mikhrin, A. Kovsh, L. West, C. Bornholdt, N. Grote and A. Zhukov, "Error-free 10 Gbit/s transmission using

individual Fabry-Perot modes of low-noise quantum-dot laser," Electron. Lett. 43(25), 1430-1431 (2007).

17. A. Capua, L. Rozenfeld, V. Mikhelashvili, G. Eisenstein, M. Kuntz, M. Laemmlin, and D. Bimberg, "Direct correlation between a highly damped modulation response and ultra low relative intensity noise in an InAs/GaAs quantum dot laser," Opt. Express 15(9), 5388-5393 (2007).
18. http://www.innolume.com/products/Gain-chips.htm.
19. Y. Zhang, S. Yang, H. Guan, A. E.-J. Lim, G.-Q. Lo, P. Magill, T. Baehr-Jones, and M. Hochberg, "Sagnac loop mirror and micro-ring based laser cavity for silicon-on-insulator," Opt. Express 22(15), 17872-17879 (2014).

Chapter 5

CONCLUSION

This thesis focuses on addressing the challenge of laser integration in the silicon photonics platform. I started with an introduction to silicon photonics technology and a review of the state-of-the-art devices, including submicron silicon waveguides, silicon electro-optic modulators, germanium-on-silicon photodetectors, and approaches for laser integration on silicon. Then Maxwell's equations, mode solving, mode overlap integral and finite difference time domain (FDTD) method are covered, which serve as the theoretical foundation of integrated optics device design. In particular, particle swarm optimization is coupled with FDTD to very effectively generate optimal device geometries. A novel grating coupler that utilizes germanium to break the symmetry of the refractive index distribution atop and beneath the silicon gratings is proposed. Since the germanium is grown in the same step as building photodetectors, no extra fabrication step is required. A germanium-assisted grating coupler design with 76% coupling efficiency and 40 nm 1 dB optical bandwidth is reported.

High performance hybrid external cavity lasers are demonstrated in Chapter 3. The gain medium is integrated by edge-coupling a reflective semiconductor optical amplifier to the silicon photonics chip. Compared to IIIV on silicon heterogeneous epitaxy or wafer bonding, this approach provides a mature, high-quality gain block and maintains the CMOS compatibility of the silicon photonics processes, resulting in the most viable solution in the near to mid future. Half-laser cavity designs on silicon

based on an eye-shaped reflector and a Sagnac-loop-based mirror are proposed. A hybrid laser working at 1570 nm, with less than 220 kHz linewidth, over 45 dB side mode suppression ratio and less than -135 dB relative intensity noise is demonstrated. An O-Band version of the device lasing at 1302 nm is also demonstrated for short reach communication applications. Open eye diagrams are demonstrated for 10 Gb/s and 40 Gb/s using the hybrid laser as the light source. A microring resonator is used in both devices as an intra cavity wavelength filters. However, the ring resonant wavelength of the ring drifts as temperature changes. A ring-resonance wavelength stabilization scheme using band-gap temperature sensor and closed-loop feedback control is also demonstrated.

Microring resonators are unique to the silicon photonics due to the high index contrast between silicon and silicon oxide. They offer compact device footprint and a variety of functions, such as wavelength filtering, multiplexing and modulation. More over, due to the periodic nature of their resonances, they inherently support wavelength division multiplexing. A multi-wavelength laser is critical to a microring based WDM system, but still remains elusive in the literature. I report a multi-wavelength external cavity laser based on a quantum dot semiconductor optical amplifier (SOA) and a silicon photonics chip. Quantum dot SOAs exhibit low mode partition noise due to their strong spectral-hole burning. Four major lasing peaks from a single cavity with less than 3 dB power non-uniformity are measured, and error-free 4×10 Gb/s data transmission is demonstrated.

The lasers presented in this thesis represent the state of the art at the time of writing. The roadmap of future work on laser integration is driven by both the laws of physics and the economics of each technical solution. Monolithic integration of optics

and electronics used to be considered an attractive idea, but turned out not to be economically competitive due to the feature size, and as a result, cost, difference. Photonics devices are on the order of tens of microns to a few millimeters, while state-of-the-art transistors have sizes down to less than 40 nm. In the short to near future, lasers are most likely to be integrated by the SOA coupling approach as I do here. Substantial progress will be made on alignment and packaging, which will include both device-level innovations, for example, edge couplers with large tolerance to mis-alignment, and improved or even customized packaging tools. In the long run, monolithic lasers based on heterogeneous epitaxy or wafer bonding may turn out to be the winning solution. Either IIIV epitaxy on silicon or subsequent processing of bonded III-V film inevitably reduces the CMOS compatibility of silicon photonics process flow. However, the exponentially increasing data traffic on the Internet drives demand for more and more high-speed, low-cost and low-energy-consumption optical interconnects. So the market volume may eventually be able to support small to mid size fabs to focus on hybrid processes for optical applications.

Regarding the laser performance, two fundamentally very challenging tasks are wavelength reference and isolation. In many applications, metro and long haul in particular, lasing wavelengths are required to fall on the ITU grid to support dense WDM. However, due to the sensitivity to fabrication variation, the microring intra cavity wavelength filter can only be lithographically controlled to a few nanometers, which is far from the requirement of single-digit GHz drift. Either an innovative on chip reference or hybrid integrated etalons will be needed. Also, laser operation is known to be sensitive to optical reflections back into the cavity. In a discrete-components-based system, an isolator is inserted between the laser and the rest of the

optical system. Because the permittivity of materials in the silicon photonics system is symmetric, light transmission is reciprocal, so an isolator is very challenging. Cascaded modulators with a specific phase delay between them can create a time-varying permittivity, which could be used to achieve a certain level of isolation. Isolator on silicon are still in their infancy, and significant breakthroughs are needed to pave the way for low loss and broadband practical isolators.

Despite existing limitations, the silicon photonics technology is believed to have a bright future, and early commercialization has begun. Note that the first transistor was demonstrated in germanium, and compound semiconductors such as GaAs have high carrier mobility, which results in better device performance. Silicon wins as the dominating integrated circuit substrates because it supports high device yield and performance uniformity. In our life today, high definition video, social media, mobile devices, cloud computing, Internet of things, etc. gets more and more popular. They all generate a large amount of data and an accelerating need for high speed, low cost, and low energy consumption communications. The demand will only grow in the future, which will drive the technology to move forward, as it has been doing for the integrated circuits for decades.

Appendix A

LIST OF PUBLICATIONS

1. **S Yang**, Y Zhang, T Baehr-Jones, M Hochberg, “High efficiency germanium-assisted grating coupler,” Opt. Express 22(25) 30607-30612 (2014)
2. **S Yang**, Y Zhang, D Grund, G Ejzak, Y Liu, A Novack, D Prather, A E-J Lim, G-Q Lo, T Baehr-Jones, M. Hochberg, "A single adiabatic microring-based laser in 220 nm silicon-on-insulator," Opt. Express 22 (1), 1172-1180 (2014)
3. **S Yang**, Y Zhang, Q Li, X Zhu, K Bergman, P Magill, T Baehr-Jones, and M Hochberg, “Quantum dot semiconductor optical amplifier/silicon external cavity laser for O-band high-speed optical communications,” Opt. Eng., 54(2), 026102 (2015)
4. **S Yang***, Y Zhang*, X Zhu, Q Li, H Guan, P Magill, K Bergman, T Baehr-Jones, and M Hochberg, “Quantum dot SOA/silicon external cavity multi-wavelength laser,” Opt. Express 23(4) 4666-4671 (2015) **contributed equally*
5. **S Yang**, A Novack, Y Ma, R Shi, M Hochberg, T Baehr-Jones, “Silicon photonics systems – nonidealities and nonlinearilities,” Optical Fiber Communications Conference, paper W1B.4 (2015)
6. **S Yang***, X Zhu*, Y Zhang, Y Li, T Baehr-Jones, M Hochberg, K Bergman, “Thermal stabilization of a microring resonator using bandgap temperature sensor,” Submitted to IEEE Optical Interconnects Conference (2015) *contributed equally
7. Y Zhang, **S Yang**, H Guan, A E-J Lim, G-Q Lo, P Magill, T Baehr-Jones, M Hochberg, “Sagnac loop mirror and micro-ring based laser cavity for silicon-on-insulator,” Opt. Express 22(15), 17872-17879 (2014)
8. Y Zhang, **S Yang**, Y Yang, M Gould, N Ophir, A E-J Lim, G-Q Lo, P Magill, K Bergman, T Baehr-Jones, M Hochberg, “A high-responsivity floating germanium photodetector,” Opt. Express 22(9), 11367-11375 (2014)
9. Y Zhang, **S Yang**, A E-J Lim, G-Q Lo, C Galland, T Baehr-Jones, M. Hochberg, "A compact and low loss Y-junction for submicron silicon waveguide," Opt. Express 21 (1), 1310-1316 (2013)
10. Y Zhang, **S Yang**, A E-J Lim, G-Q Lo, C Galland, T Baehr-Jones, M Hochberg, "A CMOS-compatible, low-loss, and low-crosstalk silicon waveguide crossing," IEEE Photon. Technol. Lett 25 (5), 422-425 (2013)

11. Y Zhang, **S Yang**, A E-J Lim, G-Q L, T Baehr-Jones, M Hochberg, “Sagnac loop mirror based laser cavity for silicon-on-insulator,” IEEE Optical Interconnects Conference, 77-78 (2014)
12. Y Ma, Y Zhang, **S Yang**, A Novack, R Ding, A E-J Lim, G-Q Lo,T Baehr-Jones, M Hochberg "Ultralow loss single layer submicron silicon waveguide crossing for SOI optical interconnect," Opt. Express 21 (24), 29374-29382 (2013)
13. Y Zhang, X Sang, **S Yang**, L Rao, W Li, J Yuan, X Xin, C Yu, “Performance analysis of dual-pump optical parametric amplifiers in silicon waveguide,” Optics Communications 15, 3043 (2010)
14. Y Zhang, M Streshinsky, A Novack, Y Ma, **S Yang**, A E-J Lim, G-Q Lo, T Baehr-Jones, M. Hochberg, “A compact and low-loss silicon waveguide crossing for O-band optical interconnect,” SPIE OPTO, 899002 (2014)

Appendix B

GLOSSARY OF ACRONYMS

BER Bit Error Rate

BOX Buried Oxide

CMOS Complementary Metal-Oxide-Semiconductor

DBR Distributed Bragg Reflector

DCA Digital Communication Analyzer

DUT Device Under Test

FDTD Finite Difference Time Domain

FOM Figure of Merit

FSR Free Spectral Range

FWHM Full Width at Half Maximum

GaAs Gallium Arsenide

InP Indium Phosphide

$LiNO_3$ Lithium Niobate

MFD Mode Field Diameter

MPW Multi Project Wafer

NRZ Non-Return to Zero

PIC Photonic Integrated Circuit

PSO Particle Swarm Optimization

QD Quantum Dot

RSOA Reflective Semiconductor Optical Amplifier

SOI Silicon on Insulator

SMSR Side Mode Suppression Ratio

TEC Thermal-electric Cooler

WDM Wavelength Division Multiplexing